Enstrophy-based proper orthogonal decomposition for reduced-order modeling of flow past a cylinder

T. K. Sengupta,* S. I. Haider, M. K. Parvathi, and G. Pallavi
Department of Aerospace Engineering, I. I. T. Kanpur 208 016, India†
(Received 21 October 2014; published 15 April 2015)

Here proper orthogonal decomposition (POD) modal decomposition are performed for flow past a circular cylinder at supercritical Reynolds numbers by projecting this onto instability modes. The important task of modeling a cylinder wake by Stuart-Landau (SL) and the Stuart-Landau-Eckhaus (SLE) equation for instability modes is discussed, with the latter shown to be more consistent with multimodal pictures of POD and instability modes. The difficult task of finding the coefficients of the SLE equation is reported by taking a least squares approach for the reduced order model (ROM). The important aspect of the ROM is the choice of initial condition for the developed SLE equations, as these are stiff ordinary differential equations which are very sensitive to the choice of initial conditions. An accurate representation of enstrophy-based POD also reveals the presence of modes which occur in isolation (in comparison to modes that come in pairs) and the traditional approach of treating instability modes by SL or SLE equations does not work directly, which also reveals higher frequency variations. Quantifying effects of this mode by time-averaged Navier-Stokes equation (NSE) fail to show the variation of the phase of these isolated time-varying modes and this is captured here using direct numerical simulation (DNS) data by a multitime scale approach. A reconstructed 3-mode ROM solution and the disturbance vorticity from DNS match globally in the flow. The agreement between 3-mode SLE reconstruction and DNS also proves the consistency of the proposed method and helps explain the physical nature of the ensuing Hopf bifurcation following an instability.

DOI: 10.1103/PhysRevE.91.043303 PACS number(s): 47.10.ad, 47.10.Fg, 47.20.Ky, 47.27.ek

I. INTRODUCTION

The Bénard-Kármán vortex street commonly observed in flow past a circular cylinder is a classic example of external flows suffering linear temporal instability. This vortex shedding is triggered by the primary instability followed by moderation of growth by nonlinear actions. In simulating unstable flows from the first principle, it is desirable to first obtain an equilibrium flow, as is the case of a zero pressure gradient boundary layer forming over a flat plate, whose receptivity and instability is traditionally studied. However, obtaining a steady equilibrium flow by solving NSE is not always guaranteed to be successful. For example, steady equilibrium flow past a wedge experiencing an adverse pressure gradient is difficult to obtain by DNS, especially with high accuracy numerical methods which are not affected by numerical diffusion. Flow past a circular cylinder also falls into this category. From an impulsive start of the flow given by inviscid flow solution, early stages of the flow evolution display a reflection symmetry about the horizontal plane, with a pair of separation bubbles forming on the lee side of the cylinder. For subcritical Re′s this pair of wake bubbles evolves to a steady state. In actual flows, ambient disturbances destabilize this equilibrium state for Re above a critical value (Re_{cr}).

In the literature, various authors have reported wide range of values at which vortex shedding initiates. For example, we quote from [1], where the authors have noted that "Batchelor [2] conjectured Re_{cr} to be between 30 and 40; Landau and Lifschitz [3] quoted it as 34.... The sensitive dependence of Hopf bifurcation or instability on facility-dependent disturbances becomes even more evident, when one considers the experimental results of Homann [4], who showed $Re_{cr} \approx 65$. These interesting results are also featured in Plate 2 of Batchelor [2] and in Schlichting [5]" (page 18). Such high value of Re_{cr} has been explained in detail in [1], where it is furthermore noted that in "figure 3 of Provansal *et al.* [6] and figure 6 of Sreenivasan *et al.* [7], different values of Re_{cr} are reported for cylinders with different length and diameter .... [T]he view expressed in these references is that they are due to different aspect ratios of the models, as the same tunnel was used for individual experimental cases.... However, this claim seemingly contradicts the observation in Williamson [8] that the flow remains essentially two-dimensional for $Re \leqslant 180$."

Thus, it is noted here that Re_{cr} is facility and background disturbance dependent. A combination of these two factors determines the receptivity of the flow field. In DNS, truncation and round-off errors act as seeds of disturbances. All these sources of errors in computations destabilize the growing bubble via asymmetric growth and shedding of vortices. In the present study, flow past a circular cylinder is investigated for sufficiently high Re′s for which the flow is supercritical, for which DNS does not provide an equilibrium solution. However, there are other efforts that reported results based on Newton-Raphson methods or selective frequency damping methods [9,10], which can provide equilibrium solutions of flow past a circular cylinder.

As disturbances grow, nonlinearity becomes important, moderating the growth obtained by linearized analysis, and this leads the flow to another saturated periodic state or a limit cycle. However, the spectrum indicates this as a multiperiodic flow depending upon the location of the point under observation. Even though the flow is characterized by single dominant frequency characterizing shed wake vortices. The multiperiodicity arises due to presence of multiple POD

*tksen@iitk.ac.in
†http://spectral.iitk.ac.in

and instability modes caused by the nonlinearity of the governing Navier-Stokes equation. This is also evident from the POD analysis of DNS results in [1] for this flow and for various other internal and external flows in [11,12].

The onset of primary instability is indicated when a bifurcation parameter (Re), exceeds a critical value and results in breaking the reflection symmetry and vortex is shed quasiperiodically, as shown here with the presence of limit cycles in the phase space, having finite width in Fig. 11. The multiple-periodic and quasiperiodic nature of the flow dynamics is related to the presence of multiple modes governed by the Navier-Stokes equation. The multiple modes have been obtained by POD analysis in [1,12] and here.

A contemporary system reduction strategy for fluid flows is the Koopman mode analysis [13], based on the spectral analysis of the finite-dimensional representation of the Koopman operator using the Krylov subspace method, a variant of the commonly used Arnoldi iteration. This linear mapping is equivalent to the dynamic mode decomposition (DMD) technique developed [14–16] for applications. Koopman analysis results in modes that are orthogonal in time (single frequency modes), while POD gives spatially orthogonal, multi-time-periodic modes (as explained before), which capture most of the enstrophy of the flow. The results of Koopman mode analysis and its variants in [17] show that this strategy, although successful in the initial linear growth stage and probably in the limit cycle stage, is not so successful in describing the transient disturbance growth in which the frequency of large scale oscillations is no longer approximately constant. POD modes, being free from any restriction on the frequency composition, are effective in capturing transient dynamics, as shown in [1] and here.

Here we successfully explore further the conversion of the problem of solving the Navier-Stokes equation (taking hundreds of CPU hours of large clusters) into solving only a limited number of complex ordinary differential equations (that will take less than minutes). Thus, we are studying the supercritical flow past a cylinder by solving equivalent ordinary differential equations, a goal in ROM for bluff body flows. Also, one can highlight the physical role played by the anomalous modes by relating POD and instability modes. Apart from explaining the role of this type of modes in taking the dynamical system to a new equilibrium state, characterized by vortex shedding, the ROM can assist in controlling such flows; e.g., suppression of vortex shedding behind cylinder [18] would be extremely beneficial to understand for scientific and technological reasons.

This paper is formatted in the following manner. In the next section, the POD modes and their classifications into regular and anomalous modes are described along with the relationship between POD and instability modes. The relevance of various governing equations for instability modes given by Stuart-Landau (SL) and Stuart-Landau-Eckhaus (SLE) are also introduced here. In Sec. III, governing equations and numerical methods are described very briefly and this is followed by a description of enstrophy-based POD method using DNS data in Sec. IV. SLE equations are described in detail in Sec. V. Also, the relationship between instability modes and SLE equation is discussed here. Actual formulation of SLE equations and their modeling is described in Sec. VI, explaining the role of the least squares approach adopted in the present investigation. Reconstruction of instability modes using the SLE equations is described in Sec. VII, including the importance and role of anomalous modes. In Sec. VII A, another aspect of the present work in modeling anomalous mode of the first kind (T_1-mode) is explained and its similarity and differences from the shift mode [19] are shown. Reconstruction of T_1 mode is the subject of discussion in Sec. VII B. The collation of the entire modeling effort in finally reconstructing the disturbance vorticity field is shown in Sec. VIII. The paper closes with a summary and conclusion.

II. PRELIMINARIES OF POD AND INSTABILITY MODES: GOVERNING EQUATIONS FOR INSTABILITY MODES

In the absence of an equilibrium flow, the flow past a circular cylinder is computed until the time-asymptotic limit is reached and instantaneous disturbance field is calculated by subtracting the mean from the instantaneous DNS field. We represent the disturbance vorticity field in POD formalism as

$$\omega'(\vec{X},t) = \Sigma_{m=1}^{\infty}\, a_m(t)\, \phi_m(\vec{X}). \tag{1}$$

This decomposition is by a Galerkin approach, where $\phi_m(\vec{X})'$s are the POD eigenfunctions. The POD amplitude function $a_m(t)'$s explicitly depend upon time, while these are related implicitly to space variables via the POD eigenfunctions. Early contributions to POD [20–22] were for describing stochastic dynamical systems. However, the related concepts from singular value decomposition were noted even earlier in Pearson [23]. In [20], POD was developed in order to project any stochastic dynamical system onto an optimal reduced-order deterministic basis. POD-based studies for fluid flows were initiated by Lumley and coauthors to investigate coherent structures in turbulent flows, as recorded in [24] and later in [7,25].

Early investigators noted that ϕ_1 and ϕ_2 are phase shifted by quarter of a cycle (i.e., by 90°) and these were considered to compose the real and imaginary parts of the dominant instability mode, $A_1(t)$ for flow past cylinder. However, in [11], it was shown that flows past a cylinder and inside a lid-driven cavity display similarity to POD modes and the first two POD modes always form a conjugate pair showing a phase shift of 90°. Any such pair of modes, phase shifted by a quarter cycle, have been termed as regular or R modes here following [1,11]. However, in [19], it is shown that, following ϕ_1 and ϕ_2, there appears to be a single mode in terms of energy content, which has no pair and alters the mean flow; the authors called it the shift mode. As the authors in [19] obtained he shift mode from RANS, its phase variation was not reported. Based on the time variations of the POD amplitude functions in [1,11,12], POD modes have been classified into regular and anomalous modes. The shift mode of [19] was noted as the anomalous mode of the first kind, or the T_1 mode. Another class of modes occurring in pairs, but having qualitatively different time variations (in the form of a wave packet), has been termed as the anomalous mode of the second kind, or T_2 mode, in [1,11].

Using primitive variable formulation, attempts have been made in [19,24–28] and many other references, where governing ODEs for the POD amplitude functions, $a_m(t)'$s, have been set up by focusing on translation energy, and in many of these studies even the contribution of pressure is omitted

while deriving the equations for $a_m(t)'$s. In [1], instead the time variation of $a_m(t)$ was obtained from DNS data directly solving the Navier-Stokes equation in stream function-vorticity formulation. This assisted in classifying the POD modes based on time variation of POD amplitude functions.

The disturbance vorticity indicated by the left hand side of Eq. (1) can also be expressed in terms of another Galerkin procedure by expressing it in terms of instability modes and the corresponding eigenfunction is given, for example, in [29] by

$$\omega'(\vec{X},t) = \Sigma_{j=1}^{\infty}[A_j(t)f_j(\vec{X}) + A_j^*(t)f_j^*(\vec{X})]. \quad (2)$$

Here $A_j(t)$ is the amplitude of the jth instability mode and A_j^* is the corresponding complex conjugate. The same notation holds for the eigenfunctions given by f_j and f_j^* for the instability modes. The classification of POD modes was helped when these were related to instability modes of fluid flow. The instability modes are related to the regular POD modes by the relationship in a manner [1,12] for the amplitude and eigenfunctions for the former,

$$A_j(t) = \sqrt{\epsilon_j}[a_{2j-1}(t) + ia_{2j}(t)], \quad (3)$$

$$f_j(\vec{X}) = \frac{1}{\sqrt{\epsilon_j}}[\phi_{2j-1}(\vec{X}) - i\phi_{2j}(\vec{X})], \quad (4)$$

where $\epsilon_j = (\lambda_{2j-1} + \lambda_{2j})/\Sigma_{k=1}^{N}(\lambda_k)$ and this normalization factor is introduced to make the dimension of $A_j(t)$ the same as that of vorticity, as ϵ_j is a measure of enstrophy (as explained in [12]). This relation between POD and instability mode does not hold for anomalous modes and is introduced here in explaining the ROM developed. As compared to the work in [1,12], this relation between POD and the instability mode is further improved. We note that the POD modes and their amplitude functions are obtained here from a singular value decomposition of DNS data obtained with a significantly more refined grid than was used in [1] to focus also on the connection between the numerical errors and the resultant vortex shedding behind a cylinder by very high accuracy schemes for supercritical Re.

Once the relations between POD and instability modes are established, it is natural to look for the governing equation(s) for the instability mode(s). One of the applications of the instability mode was originally presented by Landau [30], put in the context of a weakly nonlinear theory by Stuart [31] in the following equation by considering only one mode given by

$$\frac{dA}{dt} = \sigma A - \frac{l}{2}A|A|^2, \quad (5)$$

where $\sigma = \sigma_r + i\sigma_i$ is the linear instability mode $l = l_r + il_i$, is the Landau coefficient and $A = |A|e^{i\theta}$. The parameter σ can be obtained from a global linearized theory based on NSE also, but the Landau coefficient "l" related to the nonlinear self-interaction for a cubic nonlinearity cannot be expressed from linearized NSE. This equation (5) is henceforth referred to as the SL equation here. The nonlinearity moderates or accelerates the instability growth depending on the sign of l_r and σ_r. For flow over bluff bodies, l_r is positive ($\geqslant 0$) and moderates linear theory growth, while for channel flow, l_r, is considered negative and therefore regarded to exhibit growth or instabilities via subcritical route, as explained in [29]. It is to be noted that in developing the SL equation, a parallel flow framework was used for plane Poiseuille flow [31], which is certainly not the case for flow past a circular cylinder. Thus, Eq. (5) should be viewed more as a model mimicking the flow field observed, only along selective locations in the flow field. Another drawback of SL equation is the retention of a single instability mode only. POD analyses reported in the literature [1] show that there are a large number of modes, which contribute to the total energy or enstrophy. Hence, the corresponding instability modes also would be more than one in number.

Here, POD modes (ϕ_m's) are real, while the instability modes (f_m's) are complex, as noted in Eqs. (1) and (2) for the regular or R modes. This is also true for the POD and instability amplitudes, with $a_m(t)$ as a real and $A_m(t)$ as a complex quantity for the R modes. The presence of multiple dominant instability modes has been established in [1,11,32] for internal and external flows, which suffer multiple Hopf bifurcations (described later with respect to Fig. 3).

One of the key aspects of accurate ROM is its dependence on the primary data set from which it is reconstructed. Thus, there is a need to obtain a high accuracy solution of the governing equation. In describing the 2D dynamics of a flow field, it is noted that the stream function-vorticity formulation produces an accurate solution [33], as it satisfies the mass conservation exactly. This is discussed in the following section.

III. GOVERNING EQUATIONS AND NUMERICAL METHODS

The DNS of 2D flows is carried out here by solving the NSE in the stream function-vorticity formulation given by

$$\nabla^2\psi = -\omega, \quad (6)$$

$$\frac{\partial\omega}{\partial t} + (\vec{V}\cdot\nabla)\omega = \frac{1}{\mathrm{Re}}\nabla^2\omega, \quad (7)$$

where ω is the only nonzero out-of-plane component of vorticity. The velocity is related to the stream function as $\vec{V} = \nabla\times\vec{\Psi}$, where $\vec{\Psi} = [0\ 0\ \psi]$ and Re is based on diameter of the cylinder (D) and free stream speed (U_∞), which are used as the length and the velocity scales to nondimensionalize quantities. This formulation is preferred for 2D flows due to inherent solenoidality of the velocity field for incompressible flows to ensure mass conservation. In addition, it allows one to circumvent the pressure-velocity coupling problem, as the pressure term is absent in Eq. (7).

Equations (6) and (7) are represented in the orthogonal curvilinear coordinates (ξ,η) and the governing equations are given by

$$\frac{\partial}{\partial\xi}\left(\frac{h_2}{h_1}\frac{\partial\psi}{\partial\xi}\right) + \frac{\partial}{\partial\eta}\left(\frac{h_1}{h_2}\frac{\partial\psi}{\partial\eta}\right) = -h_1h_2\omega, \quad (8)$$

$$h_1h_2\frac{\partial\omega}{\partial t} + h_2u\frac{\partial\omega}{\partial\xi} + h_1v\frac{\partial\omega}{\partial\eta} = \frac{1}{\mathrm{Re}}\left\{\frac{\partial}{\partial\xi}\left(\frac{h_2}{h_1}\frac{\partial\omega}{\partial\xi}\right) + \frac{\partial}{\partial\eta}\left(\frac{h_1}{h_2}\frac{\partial\omega}{\partial\eta}\right)\right\}, \quad (9)$$

where h_1 and h_2 are the scale factors of the transformation given by $h_1^2 = x_\xi^2 + y_\xi^2$ and $h_2^2 = x_\eta^2 + y_\eta^2$.

The no-slip boundary condition is applied on the cylinder wall via

$$\left(\frac{\partial \psi}{\partial \eta}\right)_{\text{body}} = 0,$$

$$\psi = \text{constant}.$$

These conditions are used to solve Eq. (8) and to obtain the wall vorticity ω_b, which in turn provides the wall boundary condition for Eq. (9). At the outer boundary of the domain, a uniform flow boundary condition (Dirichlet) is provided at the inflow and a convective condition (Sommerfeld) is provided on the radial velocity at the outflow.

The convection terms of Eq. (9) are discretized using the high accuracy dispersion relation preserving (DRP) compact scheme, the OUCS3 method described in [33], which provides near-spectral accuracy for nonperiodic problems. A central differencing scheme is used to discretize the Laplacian operator of Eqs. (8) and (9) and an optimized four-stage, third-order Runge-Kutta (OCRK3) method designed in [34] is employed for time marching. Equation (8) is solved using the Bi-CGSTAB method of Van der Vorst [35].

The results presented here are for Re ranging from 60 to 150, for which the flow can be treated as two dimensional, as explained in [8]. Here the simulations have been performed in a finer grid with (1001×401) points in the azimuthal and radial directions, respectively. Note that the grid resolution employed in the present study is significantly finer in the azimuthal direction than that of the previous studies in [1,11], in which a (153×401) grid was used to compute the flow. Thus, in the azimuthal direction the number of equiangular points taken for the finer grid increases from 153 to 1001, while the resolution in the wall-normal direction is kept the same for the two grids (which is $10^{-3} D$ for these low Reynolds number flows).

Having obtained the time-accurate solution of the Navier-Stokes equation for the flow field, in the following the continuing effort on ROM using POD analysis is pursued. The present POD analysis depends on using enstrophy as the L_2 norm of the flow field, as compared to kinetic energy by other researchers, e.g., as in [19,24–28].

IV. PROPER ORTHOGONAL DECOMPOSITION

In inhomogeneous flows (which are neither homogeneous nor periodic), rotational rather than translational energy of the flow field takes precedence, as flow vorticity represents the dynamics better than the corresponding velocity field. This is discussed in detail in [32,36], where, in the latter, enstrophy transport equations are developed for 2D and 3D flows to show the process of creating smaller scales. This is the motivation behind employing an enstrophy-based POD, practiced earlier in [1,11,12,32,37,38], as compared to the energy-based POD, to identify coherent structures for flow instabilities and control studies. The dominant modes obtained through enstrophy-based POD is represented notationally based on enstrophy contents of the modes; i.e., lower numbered modes have higher enstrophy. These modes capture the dynamics of the flow more effectively for inhomogeneous flows due to the importance of rotationality of flows to explain enstrophy cascade without any assumption on the dimensionality of the flow [36]. The universality of POD modes based on enstrophy for flow past a cylinder and the flow inside a lid-driven cavity has been shown [11], making the case of using enstrophy as more relevant for vortex-dominated flows. In [12], enstrophy-based POD analysis of transitional flow past a flat plate was also reported successfully even in the primary instability stage, where there were no distinct vortices in the flow. In this instability of flow past a flat plate, a preponderance of T_2 modes has been noted.

There is another difference of the methodology adopted here for POD analysis with some of the previous efforts [19,39,40], where the dynamical model for $a_m(t)'$s are obtained through a Galerkin projection on the RANS equation and its unsteady version (URANS). These involve modeling fluctuations through Reynolds stresslike terms, whereas no modeling is resorted here and is based on time-accurate solution of the unsteady NSE. The DNS is performed by using a compact scheme for convective acceleration terms and an optimized Runge-Kutta time integration scheme has been used for the local acceleration term, with other details as given in [33]. Other recent works [41,42] explore system reduction strategies to reduce and develop models for the dynamic degrees of freedom in Galerkin systems of incompressible fluid flows based on *finite-time thermodynamics closure*. Thus, instead of developing ODEs for $a_m(t)'$s, these are directly obtained here from DNS data using the method of snapshots presented by Sirovich [25]. This involves computation of $a_m(t)'$s as an inner product of ω' with $\phi_m(\vec{X})$, suitably normalized [1,11,12].

POD as developed in [22–22,24] for a random field, $w_i(\vec{X},t)$, involves projecting it onto a deterministic set of vectors, $\phi_i(\vec{X})$, so that $\langle|(w_i,\phi_i)|^2\rangle$ is maximized, where the outer angular bracket represents a time-averaging operation and the inner bracket represents an inner product. In recent times POD has been used to study spatiotemporal dynamics of deterministic flows for flow instability [12]. Computation of $\phi_i(\vec{X})$ can be posed as an optimization problem in variational calculus, which reduces to

$$\iint R_{ij}(\vec{X},\vec{X}')\,\phi_j(\vec{X}')\,d^2\vec{X}' = \lambda\,\phi_i(\vec{X}). \tag{10}$$

The kernel of this equation is the two-point correlation function, $R_{ij} = \langle w_i(\vec{X}) w_j(\vec{X}')\rangle$, of the random field. Classical Hilbert-Schmidt theory applies to flows with finite energy, and therefore denumerably infinite orthogonal POD modes can be computed. Since the flow instabilities derive their energy from a finite source, the disturbances always remain finite and do not create a problem of applicability of the Hilbert-Schmidt theory. This is the basis of studying flow instabilities using POD [12].

Even for moderate grid resolutions, the eigenvalue problem of Eq. (10) becomes intractable. The method of snapshots was thus introduced by Sirovich [25] to overcome difficulties associated with large data sets in multiple dimensions. In this approach, the eigenfunction $\phi_m(\vec{X})$ is expressed as a linear combination of the instantaneous flow fields at distinct time instants, $t_i{}'$s,

$$\phi_m(\vec{X}) = \Sigma_{i=1}^{N}\, q_{mi}\, \omega'(\vec{X},t_i), \tag{11}$$

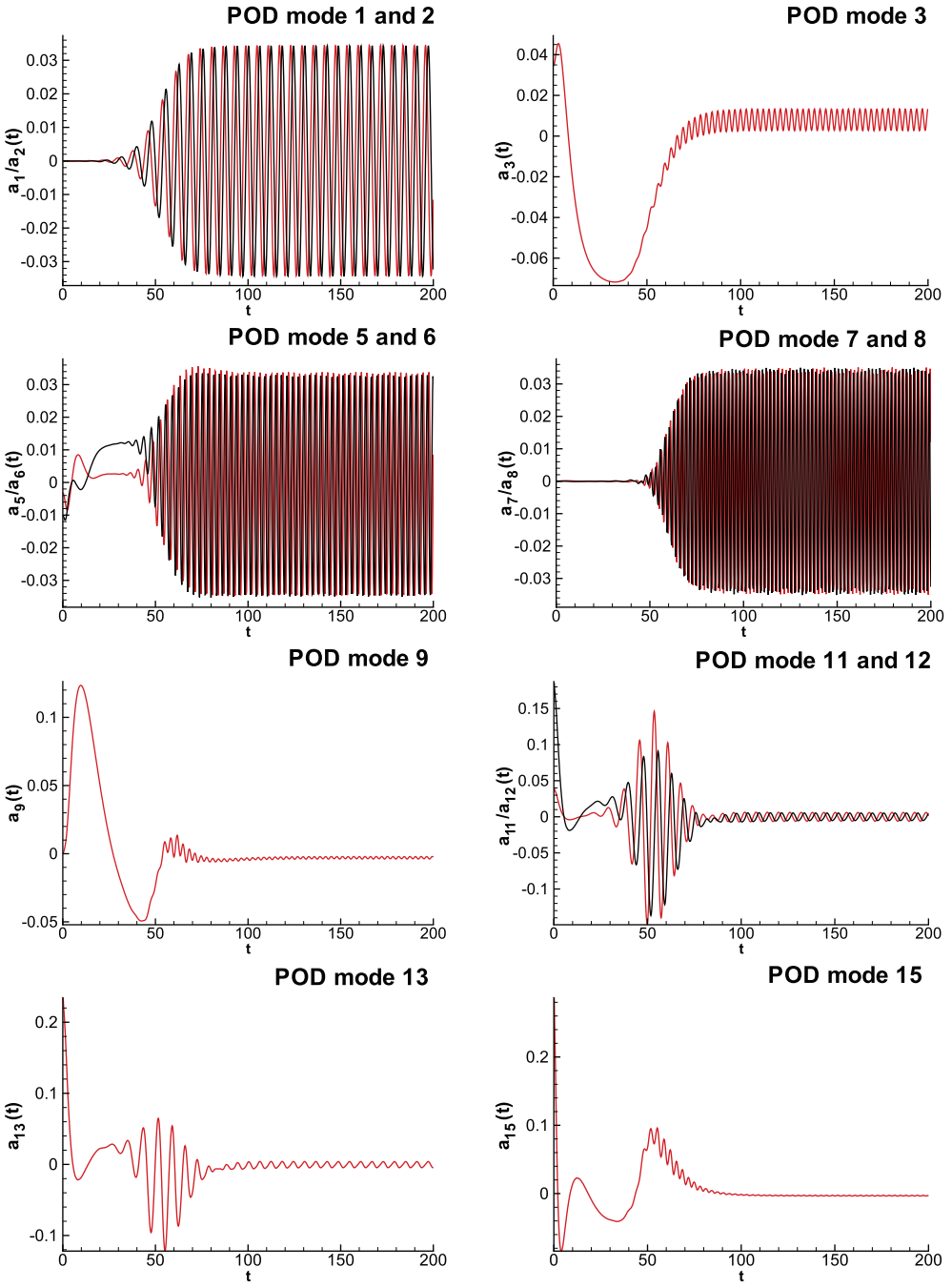

FIG. 1. (Color online) First 16 amplitude functions of Re = 100 including the missing ones, as described in [1].

where N is the number of snapshots used. This ansatz, together with the expression for R_{ij}, reduces Eq. (10) to an algebraic eigenvalue problem,

$$[C]\{\mathbf{q}\} = \lambda\{\mathbf{q}\}, \tag{12}$$

where

$$C_{ij} = \frac{1}{N}\iint \omega'(\vec{X},t_i)\,\omega'(\vec{X},t_j)\,d^2\vec{X}, \tag{13}$$

with $i,j = 1,2\ldots,N$, are defined over all the snapshots of the flow. The amplitude function $a_m(t)$ is obtained from the orthogonality property of POD eigenfunction from

$$a_m(t) = \frac{\iint \omega'(\vec{X},t)\,\phi_m(\vec{X})\,d^2\vec{X}}{\iint \phi_m^2(\vec{X})d^2\vec{X}}.$$

In the present work, POD analysis has been performed for all Reynolds numbers using 2000 snapshots from $t = 0$ to 400. The amplitude function $a_m(t)$ and the corresponding eigenfunction $\phi_m(\vec{X})$ obtained for Re = 100 are shown in Figs. 1 and 2, respectively. In Fig. 1, the first two modes form a pair that satisfies Eq. (5) and is the regular or R mode [1,11]. The modes are numbered in decreasing order of their enstrophy contents and the missing numbers (4, 10, 14, and 16)

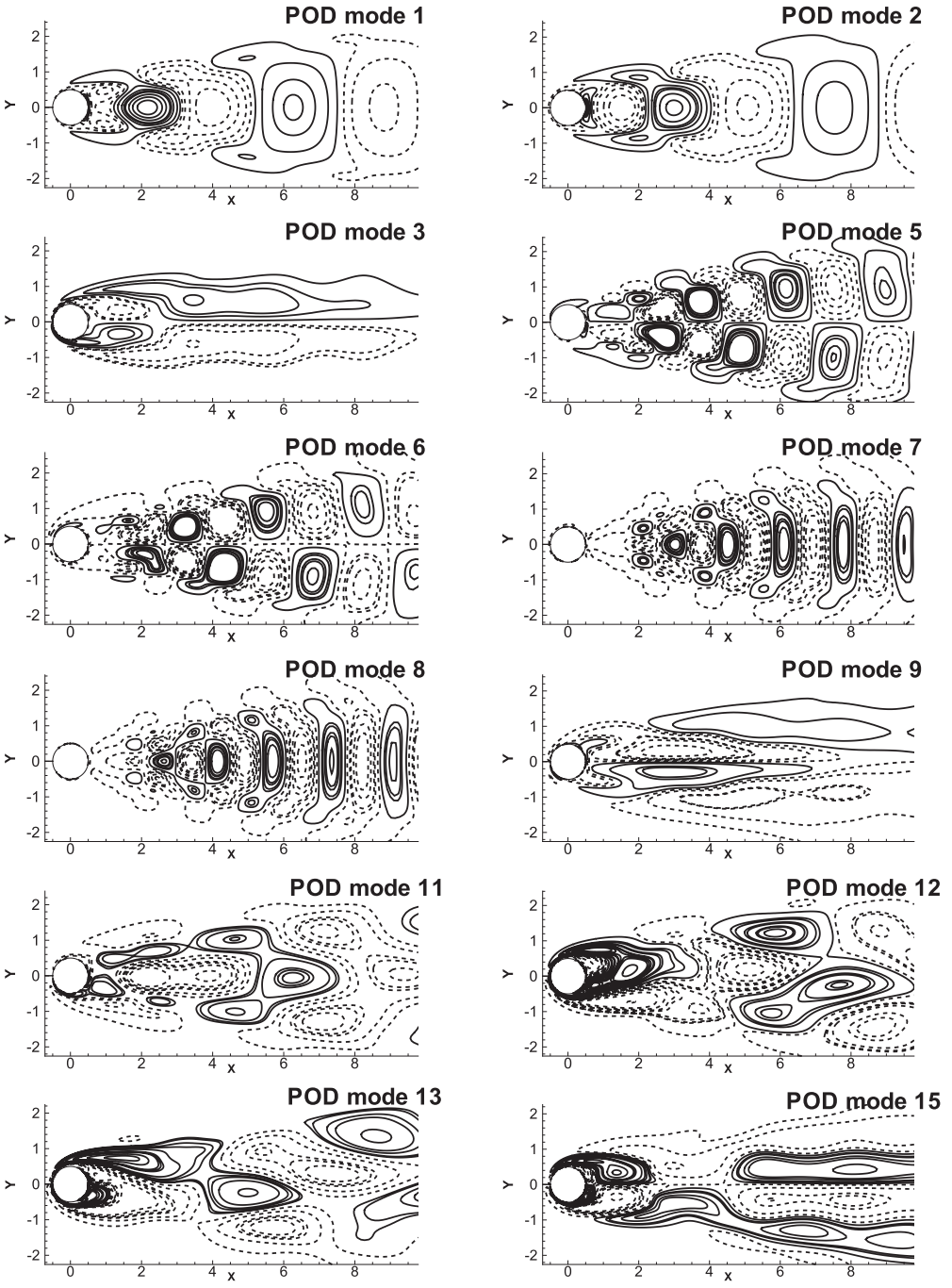

FIG. 2. First 16 eigenfunctions of Re = 100 including the missing modes, as described in [1].

represent the missing pair of the predecessor, which occurs in isolation. For example, the third POD mode has no pair, and to indicate this absence we keep the mode-4 as the missing one. In [19], only the first isolated POD mode was identified and termed as the shift mode. According to the notation here and in [1], this is a T_1 or anomalous mode of the first kind. While in [19], there was only one shift mode, in Fig. 1 one notices the multiplicity of the T_1 mode.

In Fig. 1, it is noted that this third mode is slaved at twice the Strouhal frequency, while the first two POD modes are at the Strouhal frequency. The time variation of the third mode is physically relevant, as this mode arises from the Reynolds stresslike term originating from the product of two fluctuating quantities, as shown in [1,19]. If the individual perturbation quantities are at Strouhal frequency, the product of two such fluctuating terms will necessarily be at twice the Strouhal frequency. Such products also have a time-independent component (as shown in [1]), which affects the mean flow. The results reported here show the presence of other isolated POD modes, whose amplitude functions will not satisfy the SL Equation (5) and all of these have been collectively termed as anomalous modes. This is the reason that $a_4 \equiv 0$ and $\phi_4 \equiv 0$ in this nomenclature scheme. The following two modes again constitute a regular mode pair, with the phase

variation at twice the Strouhal frequency. As the governing NSE is nonlinear, it is natural that higher superharmonics and subharmonics will show their presence. It is readily noted that modes 7 and 8 constitute the third regular mode and its phase variation is at thrice the Strouhal frequency. Thus, POD analysis clearly indicates the role of nonlinearity in deciding upon the dynamics of the system in the form of multimodal behavior, limit cycles, and multiple bifurcations, as explained with respect to Figs. 1, 4, and 5. Linearized global instability analysis would not be able to infer the effects of such modes arising from nonlinearity. The ninth mode is again a T_1 mode with phase variation given by twice the Strouhal frequency, similar to the third mode (T_1 mode). Introduction of the shift [19] or T_1 mode [1] is equivalent to splitting the unsteady Navier-Stokes equation into a time-averaged mean field, which is affected by the time-dependent perturbation field via a wave-induced stress that couples the two, as explained in [1].

The time variation of modes (11, 12), although paired, is different from the R modes. Such modes have been identified in [1] as the anomalous modes of the second kind, or T_2 mode. The modes (11, 12) show an initial growth phase followed by decay, which finally settles down to a constant amplitude oscillation at the Strouhal frequency, as shown in Fig. 1. It has been shown in [11,12] that this scheme of classifying amplitude functions of POD modes is universal for both internal and external flows, in terms of qualitative variation with time and satisfying SL equation for R modes and nonsatisfaction by anomalous modes. It is noted that internal flows display prominence of T_2 modes, as compared to external flows. Modes 13 and 15 in Fig. 1 are anomalous modes with asymptotic phase variation at Strouhal frequency and thus the classification scheme is not based on frequencies of amplitude functions.

Note that modes (5,6) although classified as regular, exhibit departures from regular mode characteristics, which do not behave similarly in the time range $t = 0$ to 80, with mode 6 showing oscillations about a nonzero mean to begin with and this mean eventually settles to zero at a later time. Despite such small differences, external flows during instability always displays a collection of three classes of modes (R, T_1, and T_2). The presence of such modes for different types of flows was shown in [12].

The POD eigenfunctions $\phi_m(\vec{X})'$s shown in Fig. 2 also attest to the classifications provided already with the help of the amplitude functions in Fig. 1. The first regular mode is characterized by vortical structures with complimentary sign at identical locations in the near wake and the spacing between the structures are large. The first T_1 mode eigenfunction appears alone and has a mirror antisymmetry about the wake centerline. The same is noted for mode 9. Modes 13 and 15 do not show any discernible patterns. The second and third regular mode pairs show different symmetry and antisymmetry in the near wake.

Having introduced the relation between POD and instability modes in Sec. II, in the following we describe how the instability modes for both the regular and the anomalous POD modes are treated by replacing the SL equation (valid for single mode only) with a generalized governing equation, which has been named as SLE equation. SLE equation naturally allows treatment of multiple modes and their nonlinear interactions.

V. INSTABILITY MODES AND THE STUART-LANDAU-ECKHAUS EQUATIONS

The interactions of instability modes have been earlier studied using the SLE equation in [1,11] for multimodal description of flow past a cylinder. This approach was considered as an improvement over the SL equation approach, which considers only one mode with amplitude A, and its self-interaction, as given in Eq. (5). From Eq. (5), one obtains equations governing the amplitude and the phase as given by

$$\frac{d|A|^2}{dt} = 2\sigma_r|A|^2 - l_r|A|^4, \tag{14}$$

$$\frac{d\theta}{dt} = \sigma_i - \frac{l_i}{2}|A|^2. \tag{15}$$

For flow below the critical Reynolds number ($\mathrm{Re_{cr}}$), σ_r is negative and if $l_r \geqslant 0$, any small perturbation introduced in the flow is eventually damped. However, when Re crosses $\mathrm{Re_{cr}}$, σ_r is positive and the flow experiences linear temporal instability, which according to Eq. (5) would be given by a linearized analysis. Due to the presence of cubic nonlinearity, amplitude growth as indicated by linear theory does not continue unabated; with increasing amplitude the nonlinear term gains significance (when $l_r|A|^2 > \sigma_r$) and moderates the growth rate, leading to a time-periodic equilibrium state as noted in Eq. (14). This qualitative transition from a steady state to a time-periodic state is the Hopf bifurcation. Equation (14) is directly integrable as [29]

$$|A|^2 = \frac{A_0^2}{\left(\frac{A_0}{A_e}\right)^2 + \left[1 - \left(\frac{A_0}{A_e}\right)^2\right]e^{-2\sigma_r t}}, \tag{16}$$

where A_0 is the value of A at $t = 0$. Here $A_e(= \sqrt{2\sigma_r/l_r})$ represents the asymptotic value of the solution as $t \to \infty$. The approach of A to A_e, which is independent of A_0, prompted researchers to conjecture Hopf bifurcation given by SL equation as universal and reinforced the belief that any computational method would produce same $\mathrm{Re_{cr}}$, independent of method or initial level of perturbations. For supercritical cases, σ_r can be linearized as $\sigma_r \sim (\mathrm{Re} - \mathrm{Re_{cr}})$ and thus the variation of A_e with Re is expected to be parabolic.

The fact that the equilibrium amplitude is not given by SL equation, is shown in Fig. 3(a), where equilibrium amplitude of streamwise fluctuating velocity (rms) variation plotted against Re are shown from the experiments of [43] and computations in [1]. It is evident that the time variation is not parabolic in Fig. 3(a), as would be expected from Eq. (16). Displayed disturbance quantities are for the rms value of streamwise velocity component [u_d(rms)], as reported in the experiment. Present calculations are for Eq. (8), indicating the equilibrium amplitude A_e of u_d, as defined in Fig. 3(b) for the vorticity. In Fig. 3(b), time variation of disturbance vorticity at a point along the centerline ($x = 0.504$) in the near wake is shown, which depicts the saturation of the disturbance vorticity with passage of time. This is indicated by the approximate equilibrium amplitude in the figure as $A_e(\omega')$. In Fig. 3(c), computed values of equilibrium disturbance vorticity at the same point in the centerline ($x = 0.504$) on the near wake display a variation of $|A_e|$ with Re. This is seen to consist of five intersecting parabolas, indicating a distinct sequence of

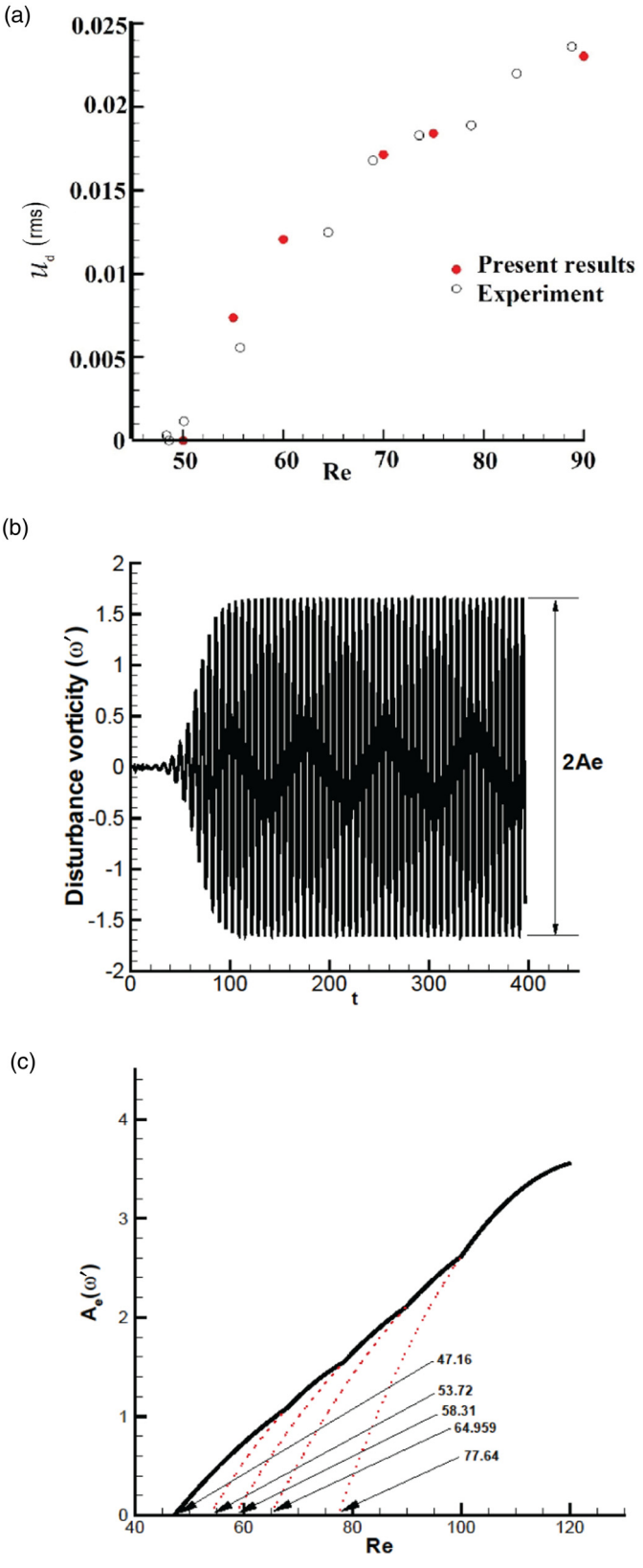

FIG. 3. (Color online) (a) Equilibrium amplitude of streamwise fluctuating velocity (rms) variation plotted against Re compared with computed data reported in [1]. (b) Time variation of disturbance vorticity at point along the centerline ($x = 0.504$) in the near wake. (c) The fluctuating vorticity equilibrium amplitude plotted as function of Re for a point at $x = 0.504$ in the near wake along the centerline.

bifurcations with Reynolds numbers. Such an observation was also noted in [1] for a less refined grid for the same flow with the help of fluctuating lift acting on the cylinder. The authors' conjecture was supported by computed data and experimental results of Homann [4], that more than one dominant mode is active during vortex shedding. While each mode is affected by various sources of ambient disturbances, it is possible to suppress the primary instability, as in the experiments of Homann [4] conducted in an oil tunnel with highly viscous fluid to attenuate disturbances and in the vortex suppression experiment reported in [43,44]. In [1], the first computed instability was noted for Re = 53.2907, the second one at the higher Reynolds number, Re = 62.5326, and a third one at Re = 78.2071.

We note the observed multiple instabilities initiated due to the presence of omnipresent disturbances, which in computations are due to numerical errors. An accurate physical DRP method will delay the onset of instabilities. Similarly, the experimental results reported in [4] with highly viscous medium damped background disturbances to bypass the first instability, and the visualization results shown in Batchelor [2] and Schlichting [5] are taken from Homann [4]. There is also the indirect evidence of suppressed instabilities for flow past a cylinder in [43,44] where the flow control was achieved by placing a smaller control cylinder in the near wake. These experimental results have been verified computationally also in [18]. The observed instability sequences in computations depend on accuracy of the numerical method used. The inaccuracies in computations are dependent upon truncation and round-off errors. While round-off error is determined by the bit precision used, the truncation error is determined jointly by the numerical method and the grid spacings.

In [1] and here a highly accurate compact scheme has been used to discretize the convective acceleration terms. For this reason in [1], only 153 points were used in the azimuthal direction and despite that the first Hopf bifurcation onset was delayed to the indicated value. In the present computations, a finer grid has been used in the azimuthal direction with 1001 points, while 401 points have been used in the wall-normal direction. Thus, the presented results would indicate how these flow instabilities are affected by the chosen grid, to help one focus on the roles played by truncation and round-off errors.

Using the 1001×401 grid here, the corresponding five critical Reynolds numbers have been obtained. Using the vorticity data on the wake centerline for Re = 55, 58, and 60, the first critical Reynolds number has been obtained as $\mathrm{Re}_{\mathrm{cr1}} = 47.16$. Similarly, using the data for Re = 70, 72, and 76, the second critical Reynolds number has been obtained as $\mathrm{Re}_{\mathrm{cr2}} = 53.72$; using the data of Re = 80, 83, and 90, the third critical Reynolds number has been obtained as $\mathrm{Re}_{\mathrm{cr3}} = 58.31$. Finally, fourth and fifth bifurcation Reynolds numbers are obtained as $\mathrm{Re}_{\mathrm{cr4}} = 64.949$ and $\mathrm{Re}_{\mathrm{cr5}} = 77.64$, respectively, using the data of Re = 92, 95, and 100 and Re = 100, 104, and 110, respectively. Thus, the use of a refined grid in the azimuthal direction by a factor of more than six times, while keeping grid spacing the same in the wall-normal direction, actually reduces the critical Reynolds numbers with respect to coarse grid simulation. In [1], the use of a (153×401) grid predicted the first critical Reynolds number as 53.2907, while the present finer grid computations using (1001×401)

points provides a critical Reynolds number around Re = 53, and with the finer grid, an additional instability is noted earlier for $\mathrm{Re}_{\mathrm{cr1}} = 47.16$.

Multiple instabilities also indicate the existence of more than one bifurcation, as stated in [1]. This aspect of multiple Hopf bifurcations was established subsequently for internal and external flows in [11]. The observations on multimodal instabilities and multiple Hopf bifurcations clearly bring out the limitation of SL equation that presumes a single bifurcation and a single instability mode. To address multiple Hopf bifurcations, one needs to account for more than one instability mode in the flow and these resulted in the use of SLE equations. General formulation of the SLE equations in [1,11] is based on the eigenfunction expansion method proposed by Eckhaus [45]. In this approach, the instability equation is given by

$$\frac{dA_j}{dt} = \alpha_j A_j + \Sigma_{k=1}^{M}\, N_j(A_k, A_j). \tag{17}$$

The last term on the right hand side accounts for the nonlinear interactions among all the M modes, inclusive of self-interaction. As suggested by Eckhaus [45] for general cases and Landau [30] for a single mode case, the nonlinear term is taken as $\beta_{jk} A_j |A_k|^2$. Thus, the M-mode SLE equations can be written as follows:

$$\frac{dA_j}{dt} = \alpha_j A_j + \Sigma_{k=1}^{M}\, \beta_{jk} A_j |A_k|^2. \tag{18}$$

Similar to the SL equation, the amplitude and phase equations can be obtained from Eq. (18) and written in the following form:

$$\frac{d|A_j|}{dt} = (\alpha_j)_{\mathrm{Re}} |A_j| + \Sigma_{k=1}^{M}\, (\beta_{jk})_{\mathrm{Re}} |A_j||A_k|^2 \tag{19}$$

and

$$\frac{d\theta_j}{dt} = (\alpha_j)_{\mathrm{Im}} + \Sigma_{k=1}^{M}\, (\beta_{jk})_{\mathrm{Im}} |A_k|^2. \tag{20}$$

Following the definition of the instability modes, the POD modes are numbered and paired as shown, in the third column of Table I, to construct the instability amplitude functions, indicated in the first column of the table for the case of Re = 100.

From Eqs. (3) and (4), instability eigenfunctions $[f_j(\vec{X})]$ and amplitude functions $[A_j(t)]$ are obtained from the POD data calculated from DNS of the flow. We have plotted the imaginary and real parts of the instability modes, with time as the parameter in phasor plots shown in Figs. 4 and 5,

TABLE I. Classification of SLE modes of Re = 100.

SLE modes	POD mode type	POD modes
A_1	Regular (R_1)	$\begin{cases} a_1 \\ a_2 \end{cases}$
A_2	Anomalous mode of type 1 (T_1)	$\begin{cases} a_3 \\ - \end{cases}$
A_3	Regular (R_2)	$\begin{cases} a_5 \\ a_6 \end{cases}$
A_4	Regular (R_3)	$\begin{cases} a_7 \\ a_8 \end{cases}$

for the flows at Re = 100 and Re = 150, respectively. The instability modes 1, 3, and 4 have been constructed from R modes; instability modes 2 and 5 are formed with T_1 modes, while instability mode 6 is formed using T_2 modes. As a consequence, instability modes A_2 and A_5 in these figures appear as straight lines along the line $\mathrm{Im}(A_2) = 0$, as these are constructed with T_1 modes. Note that the limit cycles of the regular instability modes are not circles, but annuli of finite thickness in Figs. 4 and 5. This thickness is a measure of the range of variation of the saturation amplitude.

From DNS data, one constructs $a_m(t)$ and $\phi_m(\vec{X})$ using Eq. (11). From these POD amplitudes and eigenfunctions, one obtains amplitudes and eigenfunctions, $A_j(t)$ and $f_j(\vec{X})$, of the instability modes using Eqs. (3) and (4). For example, the amplitude of the instability mode is given by

$$A_j(t) = \frac{\iint f_j(\vec{X})\, \omega'(\vec{X},t)\, d^2\vec{X}}{\iint f_j(\vec{X}) f_j(\vec{X})\, d^2\vec{X}}.$$

In Figs. 6 and 7, modulus of the instability modes are shown for Re = 100 and 150, respectively. For the first instability mode, the phase variation is at Strouhal frequency for both cases, while the amplitude has a nonzero value. This is despite the fact that the constituent POD modes, $a_1(t)$ and $a_2(t)$, have a zero mean in Fig. 1. After the initial transients, the first instability mode settles down to almost a steady value for both the Reynolds numbers. The second instability mode is made up of $a_3(t)$ and displays phase variation at twice the Strouhal number, as can be ascertained from FFT of data shown in Fig. 1. Unlike the first instability mode, this second instability mode does not settle down to a steady value. Any time-averaged view of this by RANS-like approach (as in [19,40,41]) will show only the mean shift, but will not show the phase variation. To capture this phase variation of $A_2(t)$, the present DNS-based approach can capture this clearly. In Figs. 6 and 7, the time variation of $|A_3|$ and $|A_4|$ for the next two regular modes are also shown, which display mode switching with change in Reynolds number. In the POD framework, the numerical precedence of a mode indicates its higher enstrophy content, with respect to subsequent ones. In Fig. 6 for Re = 100, mode A_3 represents higher fluctuation about the mean after the periodic equilibrium is reached, while the mode A_4 shows significantly lower fluctuations, whereas in Fig. 7, this particular role of the A_3 and A_4 modes in indicating fluctuations after second equilibrium is exchanged; i.e., the fluctuations of the A_3 mode is significantly reduced as compared to the A_4 mode. Furthermore, for Re = 100 in Fig. 6, $|A_3|$ shows phase variation at twice the Strouhal frequency and $|A_4|$ shows phase variation at three times the Strouhal frequency. In Fig. 7 for Re = 150, the phase variations of $|A_3|$ and $|A_4|$ are thrice and twice the Strouhal frequency, respectively.

However, the most important feature of Figs. 6 and 7 is the behavior of A_2 (the first T_1 mode), which shows significant phase variation at later times, while the phasor plot in Figs. 4 and 5 do not show any phase variation due to the nature of construction of $A_2(t)$ by conventional method given in Eqs. (3) and (4). This is addressed and rectified by an augmented model in the next section. The instability modes $|A_5|$ and $|A_6|$ have residual effects at large times and their phase variations are

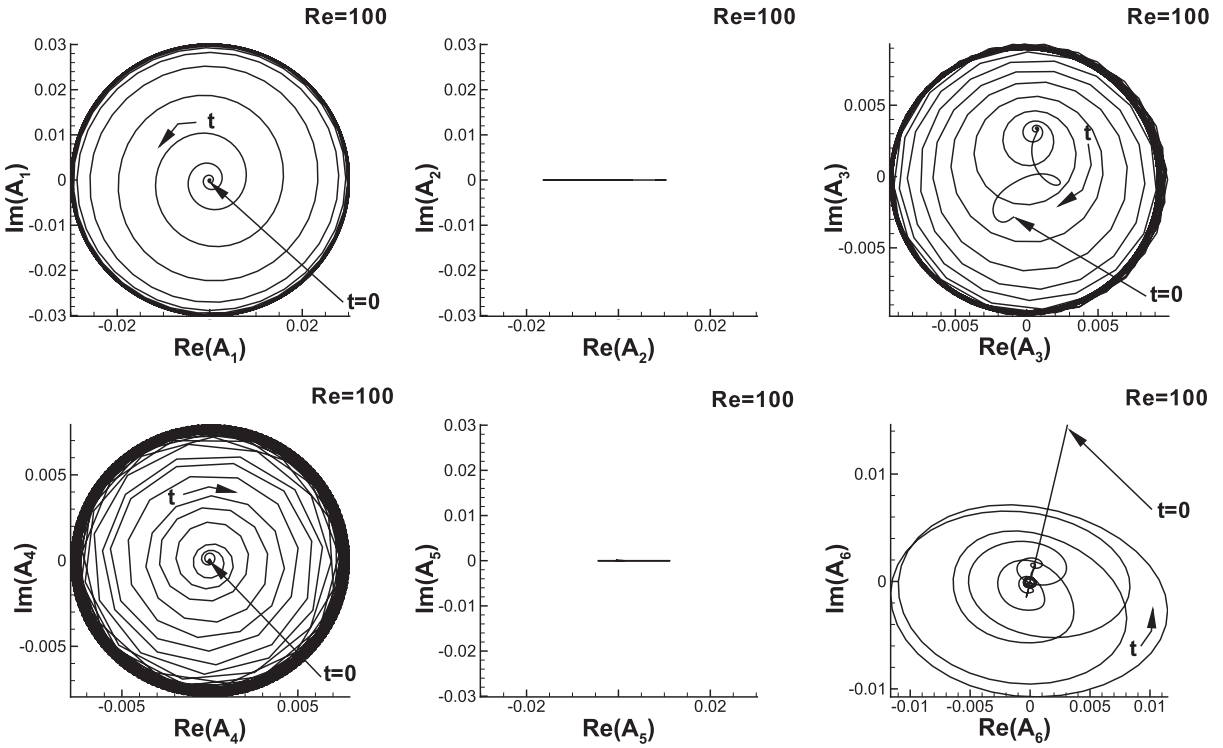

FIG. 4. Phasor plots of instability modes of Re = 100.

at twice the Strouhal frequency and at the Strouhal frequency, respectively.

Having established the relevance of multiple instability modes, it is necessary to go beyond the SL equation, which tries to explain the dynamics by a single mode. As noted already, this is the justification for providing formulation and modeling of these multiple modes. In [1], this was initiated by invoking the SLE equation. In the following, the same has been further

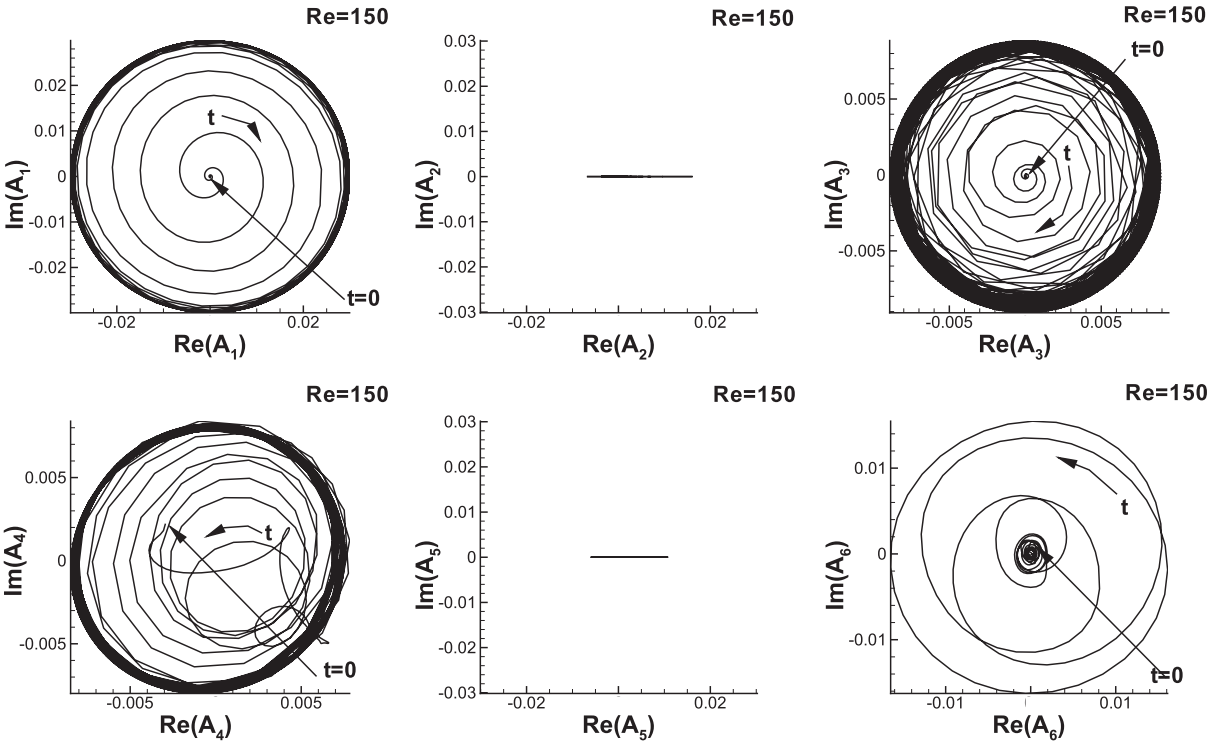

FIG. 5. Phasor plots of instability modes of Re = 150.

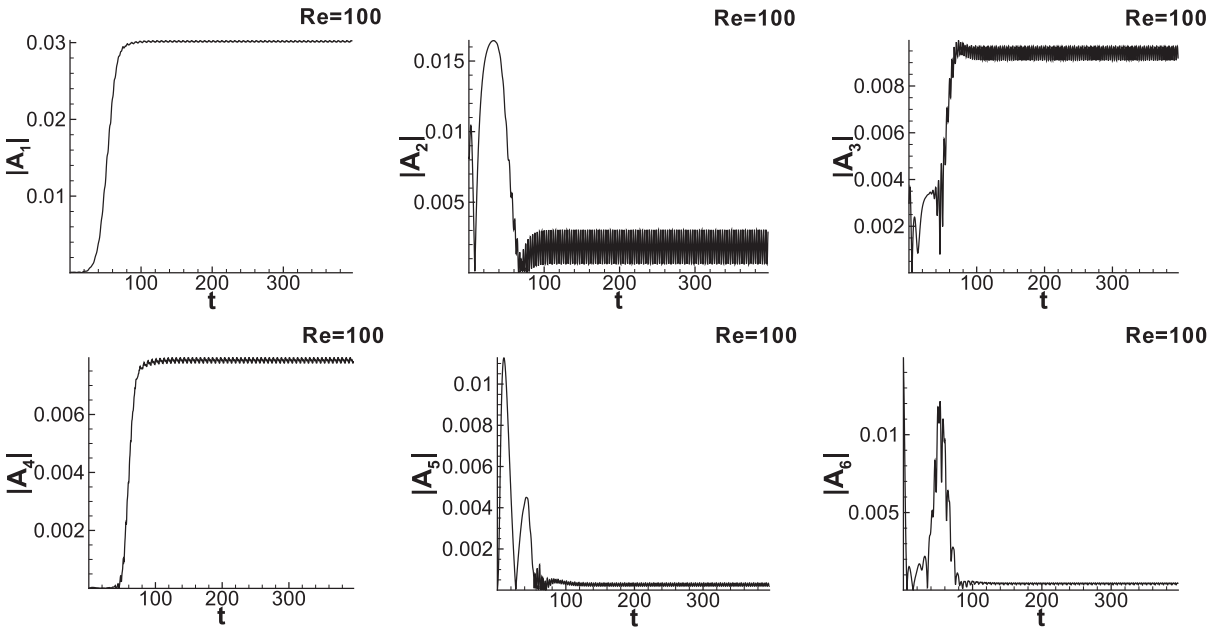

FIG. 6. Amplitude variation of the instability modes of Re = 100.

improved by obtaining a better formulation through the least squares formalism for the SLE equations.

VI. FORMULATION AND MODELING OF THE SLE EQUATION

The instability modes have characteristic phase and amplitude variations that can be readily obtained from DNS and modeled values, as in Eqs. (19) and (20). This involves obtaining the coefficients of the SLE equations governing the temporal instability growth obtained from the DNS results. In [1], these were obtained by using the temporal rates at those many time instants, as there are unknowns. However, coefficients thus obtained show large variability depending upon the chosen time sector.

A. SLE equations for $|A_j|$ and θ_j

The nonuniqueness of the values of $(\alpha)_{\mathrm{Re}}$, (α_{Im}), $(\beta_{jk})_{\mathrm{Re}}$, and $(\beta_{jk})_{\mathrm{Im}}$, depending on the value of time sector chosen, can be avoided by evaluating these coefficients as a least squares problem of an overdetermined system of linear equations by considering the full time interval, including the initial transients. The sequence of Hopf bifurcation takes the state

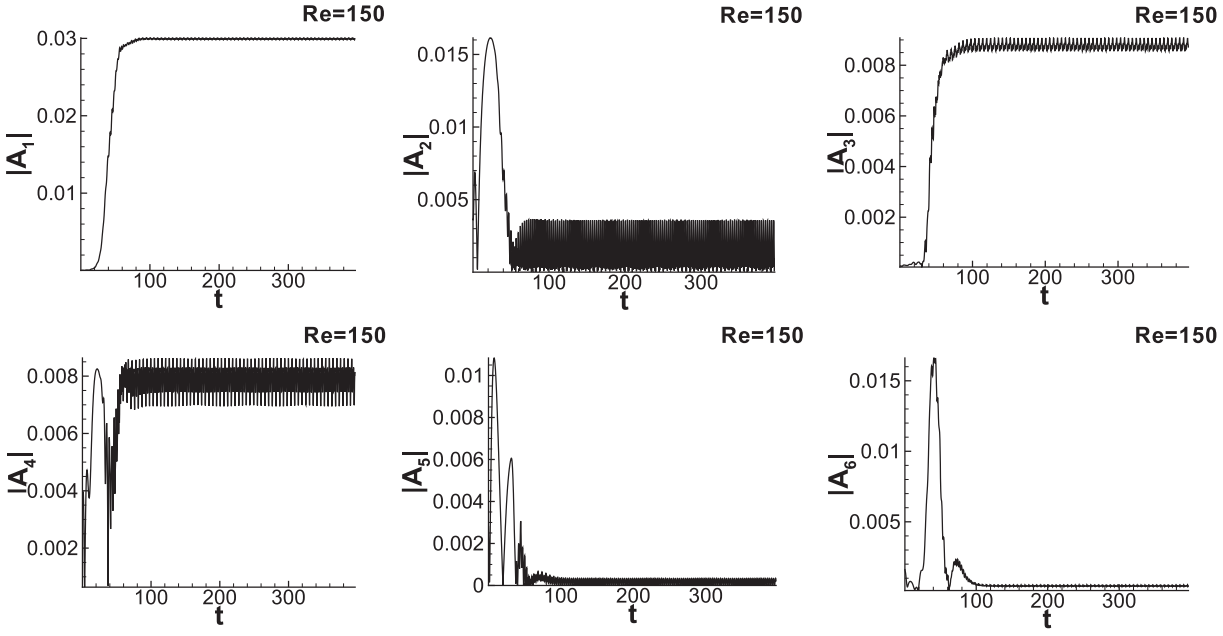

FIG. 7. Amplitude variation of the instability modes of Re = 150.

from the quiescent equilibrium condition to a periodic state (the second equilibrium state), for the flow past a circular cylinder. Thus, the second equilibrium should be characterized by a constant amplitude oscillation at the Strouhal number, as explained by Eq. (16). This does not happen necessarily, as one notes from Figs. 4 and 5 that both the amplitude and phase variations are not characterized by fixed amplitude and frequency at the second equilibrium state. This is seen from the finite thickness of the limit cycles in the phasor plots. A constant amplitude would have indicated zero thickness of the limit cycles. Relatively, the thickness of the attractor for the A_4 and A_3 modes are significantly wider as compared to that for the A_1 mode. During the transient stages, the variations are even more pronounced and a lower-order model would invariably be error prone, if one wants a deterministic evaluation of SLE model constants, as was attempted in [1]. Hence, we obtain the model constants in a least squares framework by minimizing the model error. For the M-mode SLE equation for $|A_j|$, we have $(M+1)$ unknowns as $(\alpha_j)_{\mathrm{Re}}$ and $(\beta_{jk})_{\mathrm{Re}}$, where k varies from 1 to M. The same procedure can be applied to the phase equation for θ_j. There are $N \gg M$ linear equations available, each corresponding to a time instant, where N is the number of snapshots used for POD. These equations for $|A_j|$ and θ_j are given at $t = t_i$ by

$$\frac{d|A_j(t_i)|}{dt} = (\alpha_j)_{\mathrm{Re}}|A_j(t_i)| + \Sigma_{k=1}^{M}\,(\beta_{jk})_{\mathrm{Re}}|A_j(t_i)||A_k(t_i)|^2, \tag{21}$$

$$\frac{d\theta_j(t_i)}{dt} = (\alpha_j)_{\mathrm{Im}} + \Sigma_{k=1}^{M}\,(\beta_{jk})_{\mathrm{Im}}|A_k(t_i)|^2, \tag{22}$$

where $i = 1$ to N correspond to each snapshot. Least squares approach gives us a solution that minimizes the norm of error in the set of N equations in (21) and (22). In a generic form, these set of equations can be written as

$$Q_j = \delta_j P_{1,j} + \Sigma_{k=1}^{M}\gamma_{jk}P_{k+1,j}. \tag{23}$$

For the amplitude variation,

$$Q_j = \frac{d|A_j|}{dt} \quad \text{and} \quad P_{1,j} = |A_j|,$$
$$P_{k+1,j} = |A_j||A_k|^2,$$
$$\delta_j = (\alpha_j)_{\mathrm{Re}} \quad \text{and} \quad \gamma_{jk} = (\beta_{jk})_{\mathrm{Re}}.$$

Similarly for the phase variation, the following substitutions apply:

$$Q_j = \frac{d\theta_j}{dt} \quad \text{and} \quad P_{1,j} = 1,$$
$$P_{k+1,j} = |A_k|^2,$$
$$\delta_j = (\alpha_j)_{\mathrm{Im}} \quad \text{and} \quad \gamma_{jk} = (\beta_{jk})_{\mathrm{Im}}.$$

The squared error associated with the above equation can be expressed as

$$E_j = \Sigma_{m=1}^{N}[Q_j(t_m) - \{\delta_j P_{1,j}(t_m) + \Sigma_{k=1}^{M}\gamma_{jk}P_{k+1,j}(t_m)\}]^2. \tag{24}$$

The method of least squares is used to fix the value of unknowns, δ_j and γ_{jk}, by minimizing the above error norm.

TABLE II. Coefficients of Eq. (21) for Re = 100.

j	α_j	β_{j1}	β_{j2}	β_{j3}
1	8.941×10^{-2}	-8.412×10^{1}	1.641×10^{2}	-1.504×10^{2}
2	-2.429×10^{-3}	-1.967×10^{2}	-9.148×10^{1}	2.005×10^{3}
3	5.883×10^{-4}	-3.604×10^{2}	-1.231×10^{2}	3.122×10^{3}

From the $M+1$ equations, minimizing the error norm with respect to the unknowns is obtained as follows:

$$\frac{\partial E_j}{\partial \delta_j} = 0 \quad \text{and} \quad \frac{\partial E_j}{\partial \gamma_{jk}} = 0.$$

By substituting for E_j in these equations, we get

$$\frac{\partial E_j}{\partial \delta_j} = \Sigma_{m=1}^{N}[Q_j(t_m) - \{\delta_j P_{1,j}(t_m) + \Sigma_{k=1}^{M}\gamma_{jk}P_{k+1,j}(t_m)\}]P_{1,j}(t_m) = 0, \tag{25}$$

$$\frac{\partial E_j}{\partial \gamma_{jl}} = \Sigma_{m=1}^{N}[Q_j(t_m) - \{\delta_j P_{1,j}(t_m) + \Sigma_{k=1}^{M}\gamma_{jk}P_{l+1,j}(t_m)\}]P_{k+1,j}(t_m) = 0. \tag{26}$$

The above set of $(M+1)$ linear equations can be written in the form

$$[\bar{R}]\{x\} = \{s\},$$

where $[\bar{R}]$ is a $(M+1) \times (M+1)$ matrix and $\{x\}$ denotes the $(M+1)$ unknown coefficients. The solution to this gives us the requisite coefficients of the SLE equations, δ_j and γ_{jk}. In the following section, the case of Re = 100 is treated to obtain the corresponding SLE coefficients.

VII. RECONSTRUCTION OF INSTABILITY MODES USING SLE EQUATIONS

Here results of reconstruction, using the formulation described above, are provided. Using the least squares method, the coefficients of amplitude and phase equations [Eqs. (21) and (22)] for the 3-mode, (A_1, A_2, A_3)-SLE equations are shown in Tables II and III.

Before we embark upon solving Eqs. (21) and (22), it is appropriate to note the need for initial conditions, which helps one to focus on developing a ROM that will replace the task of solving NSE with different boundary and initial conditions. Equations (21) and (22), apart from being nonlinear, are also stiff, as the original NSE for supercritical Re is stiff. One of the attributes of any stiff differential equation is its sensitive dependence on initial conditions. Thus, there is a genuine need to look for optimum initial conditions for

TABLE III. Coefficients of Eq. (22) for Re = 100.

j	α_j	β_{j1}	β_{j2}	β_{j3}
1	1.490×10^{-1}	8.849×10^{2}	2.660×10^{3}	8.706×10^{2}
2	0.00	0.00	0.00	0.00
3	-3.182×10^{-1}	-2.227×10^{3}	1.126×10^{3}	3.277×10^{3}

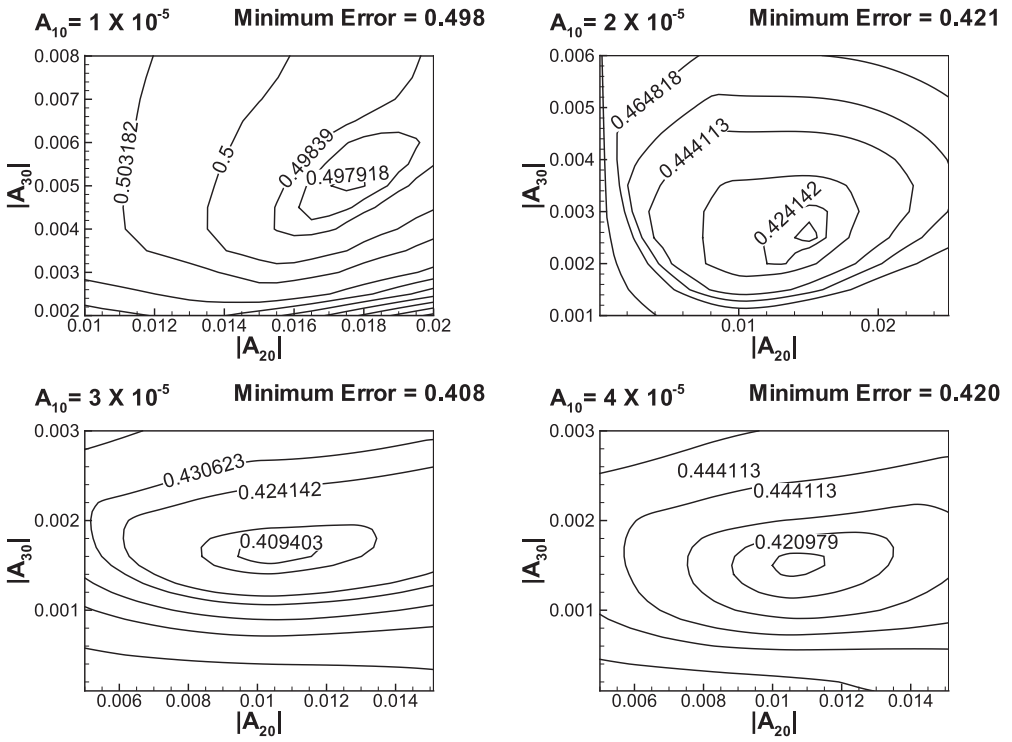

FIG. 8. Time integrated error contours for $0 < t \leqslant 396$ are plotted in the $(A_{20},\ A_{30})$ plane for different values of A_{10} for Re $= 100$.

Eqs. (21) and (22) for every Reynolds number. To locate the optimum initial conditions for the Re $= 100$ case, Eqs. (21) and (22) with coefficients given in Tables II and III, are solved for different combinations of initial conditions as given by A_{10}, A_{20}, A_{30} for a 3-mode SLE reconstruction. The reconstruction is carried out using an implicit RK_2 method [46] with a time step of 0.001. The essential idea here is to locate the optimum values for the initial conditions, for which the time integrated error norm in Eq. (24) is minimum. The reason for choosing the 3-mode SLE reconstruction is that the 2-mode SLE equation reconstruction failed for all cases with different initial conditions. Thus, the 3-mode SLE model is the minimal set for ROM for this flow. Thus, in the following, we obtain optimum conditions to compute the departure between the DNS and the simulated data by solving Eqs. (21) and (22) and using those in Eq. (2) to minimize the error in Eq. (24), summed over the full time range. Thus, the model is "trained" with known DNS data for different Reynolds numbers.

We note that replacement of an initial-boundary value problem (NSE) with a set of initial value problem would somehow require the missing information coming from the boundary conditions. This is manifested as requiring an optimal set of initial conditions for the solution of Eqs. (21) and (22) with the coefficients given in Tables II and III. Any initial condition will not be adequate to address this issue.

The following strategy has been adopted to locate the global minimum for the combination of A_{10}, A_{20}, A_{30} in order to arrive at a ROM with least error between the computed ODEs and the corresponding DNS data. In doing so, one fixes a value of A_{10}, with A_{20} and A_{30} values chosen in a grid, in the $(A_{20},\ A_{30})$ plane. Time integrated errors obtained from $t = 0$ to 396 are plotted in the $(A_{20},\ A_{30})$ plane, as shown in Fig. 8 for error contour plots for different fixed values of A_{10}. The minimum error location corresponding to different values of A_{10} in the $(A_{20},\ A_{30})$ plane are noted as local minimum. In Fig. 9, extracted local minima of error are plotted as a function of A_{10}, which helps identify the global minimum. The global minimum error of the 3-mode SLE reconstruction is given by the following initial conditions of the instability modes for Re $= 100$ as

$$A_1(0) = 3.0 \times 10^{-5},$$
$$A_2(0) = 1.05 \times 10^{-2}, \quad \text{and} \quad A_3(0) = 1.6 \times 10^{-5}.$$

With the above optimum initial conditions, Eqs. (21) and (22) are solved with the coefficients given in Tables II and

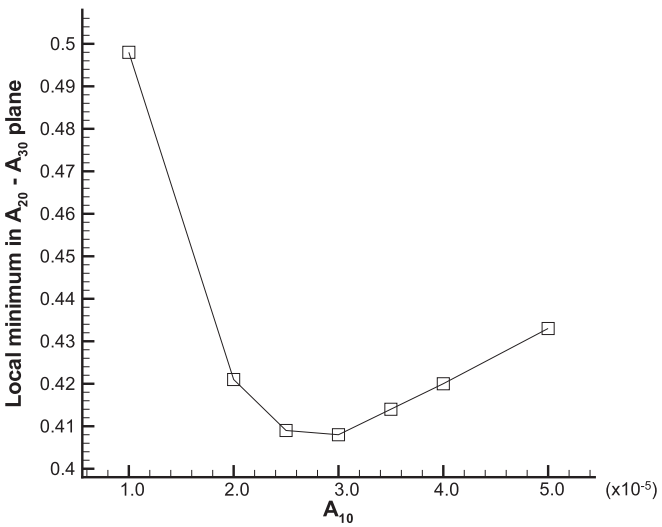

FIG. 9. Extracted minimum integrated error plotted as a function of A_{10} for Re $= 100$.

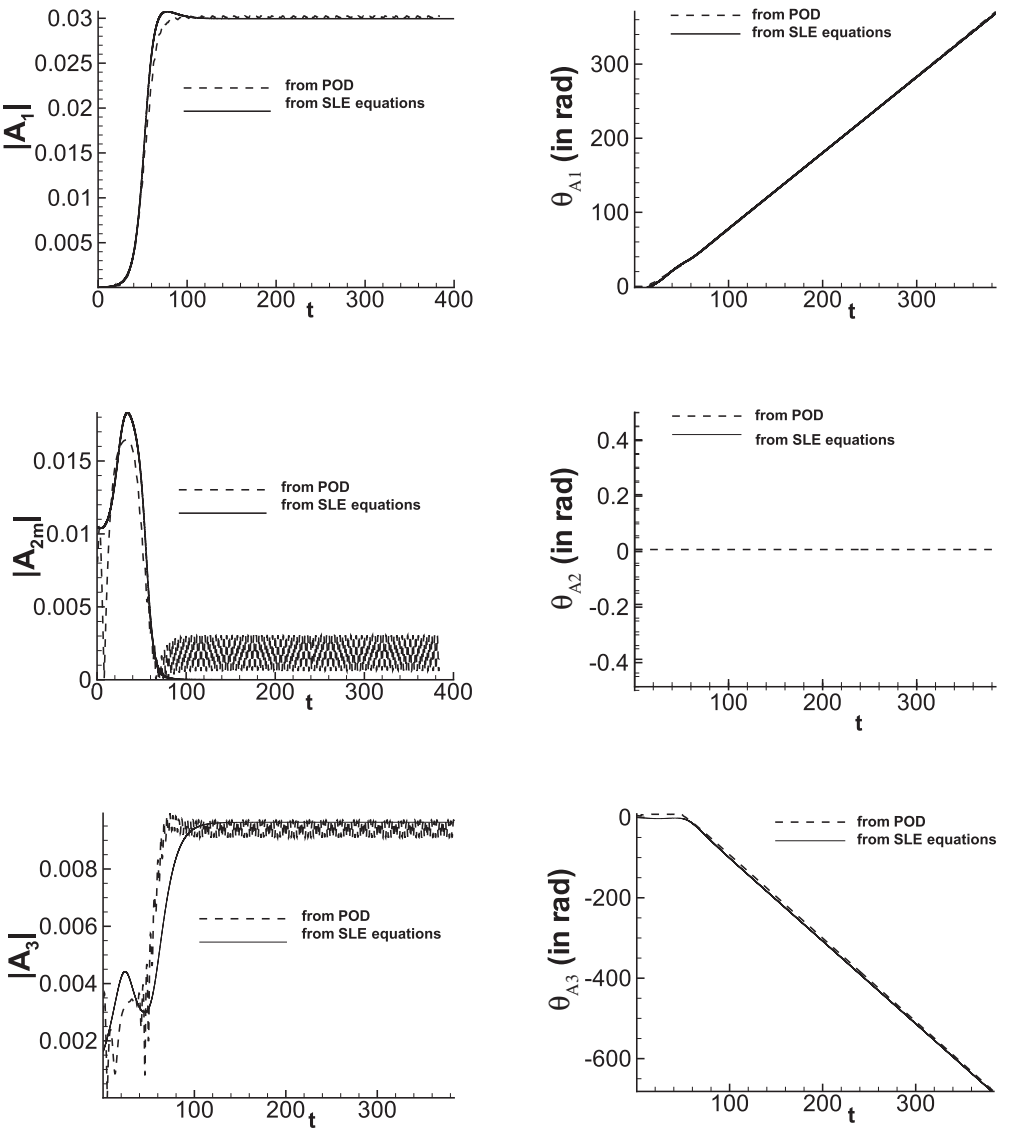

FIG. 10. Optimal reconstruction for the three-mode case for Re = 100.

III. The results of the reconstruction given in Fig. 10 show that the reconstructed amplitude variation of the regular instability modes (with A_1 and A_3) matches well with the DNS results. However, the reconstruction of the T_1 mode (A_2) is unsatisfactory for the reasons noted before. The procedure followed is simply not capable of capturing its oscillatory behavior after saturation. It must be emphasized that POD of DNS data do not lack this information. This has to do with the instability mode modeling via the SLE equation approach for the T_1 mode, which is incapable of capturing the oscillatory nature of the instability mode. Thus, in ROM there is a need to properly incorporate the oscillatory nature of T_1 modes after saturation, which is attempted next.

As with the amplitude equations, the phase equations also require specification of initial conditions for time integration. However, unlike amplitude equations, the phase variation is only laterally shifted by the initial conditions, since the phase is governed by Eq. (22). The initial condition changes the intercept of the phase variation on the $t = 0$ line, while preserving local slope values.

In light of this observation, the following methodology is adopted to find the initial conditions for phase. The time integration, with all phases initialized to zero, is carried out and subsequently results are compared with the phase variation from DNS to obtain the difference between the two $[= \theta_{\mathrm{DNS}}(t) - \theta_{\mathrm{reconstructed}}(t)]$. The time average of this difference is set as the initial phase. The initial phase values thus obtained for Re = 100 are

$$\theta_1(0) = -7.637 \text{ rad},$$
$$\theta_2(0) = 0 \text{ rad}, \quad \text{and} \quad \theta_3(0) = 7.766 \text{ rad}.$$

A. Modeling the anomalous mode of the first kind (T_1 mode)

In constructing an instability mode corresponding to a T_1 mode, it is expressed with the single POD mode, as its pair is missing. Following the traditional approach [26,27] this will result in an instability amplitude function formed by a real POD amplitude function and in the same way the corresponding eigenfunction is real. However, from Fig. 1, it

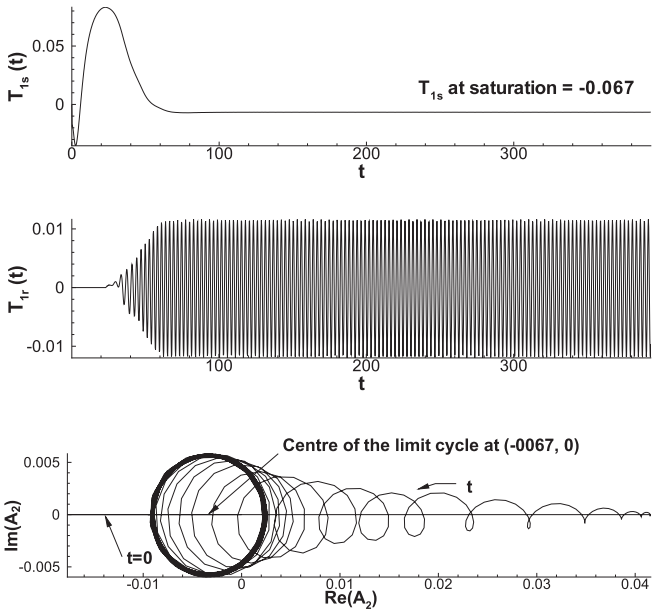

FIG. 11. The slowly varying and rapidly varying components of the T_1 mode (POD mode-3 for Re = 150) (top two panels) and the phasor plot (bottom panel) of the corresponding instability mode.

is clear that the first T_1 mode (POD mode 3 for Re = 100) exhibits oscillatory behavior at saturation, signifying phase variation. Thus, the traditional approach of constructing instability mode from POD modes will not be able to account for time-varying oscillations of T_1 modes. Thus, there is a need to have an alternative representation of the instability modes corresponding to T_1 modes. This is one of the motivations of the present work over that was presented in [1].

As noted earlier, T_1 modes obtained from the POD analysis show time-periodic behavior during and after saturation, from which it can be construed that it involves variation at two disparate time scales, a slowly varying component which accounts for the mean field correction (as in the shift mode of [19]) and a rapidly varying time-periodic component.

The present task is to devise a representation for the T_1 mode which would account for the phase variation at small time scales. A possible solution is splitting the T_1 mode into a slowly and a rapidly varying component by introducing two different time scales. The slow variation is extracted by smoothing the data by removing the fluctuating components to obtain $T_{1s}(t)$. This is performed by low pass filtering the data at postprocessing stage. This is shown in the top frame of Fig. 11 for Re = 150. The rapidly varying component T_{1r} can then be found by subtracting the slow variation from the original T_1 mode by

$$a_{T1}(t) = T_{1s}(t) + T_{1r}(t). \tag{27}$$

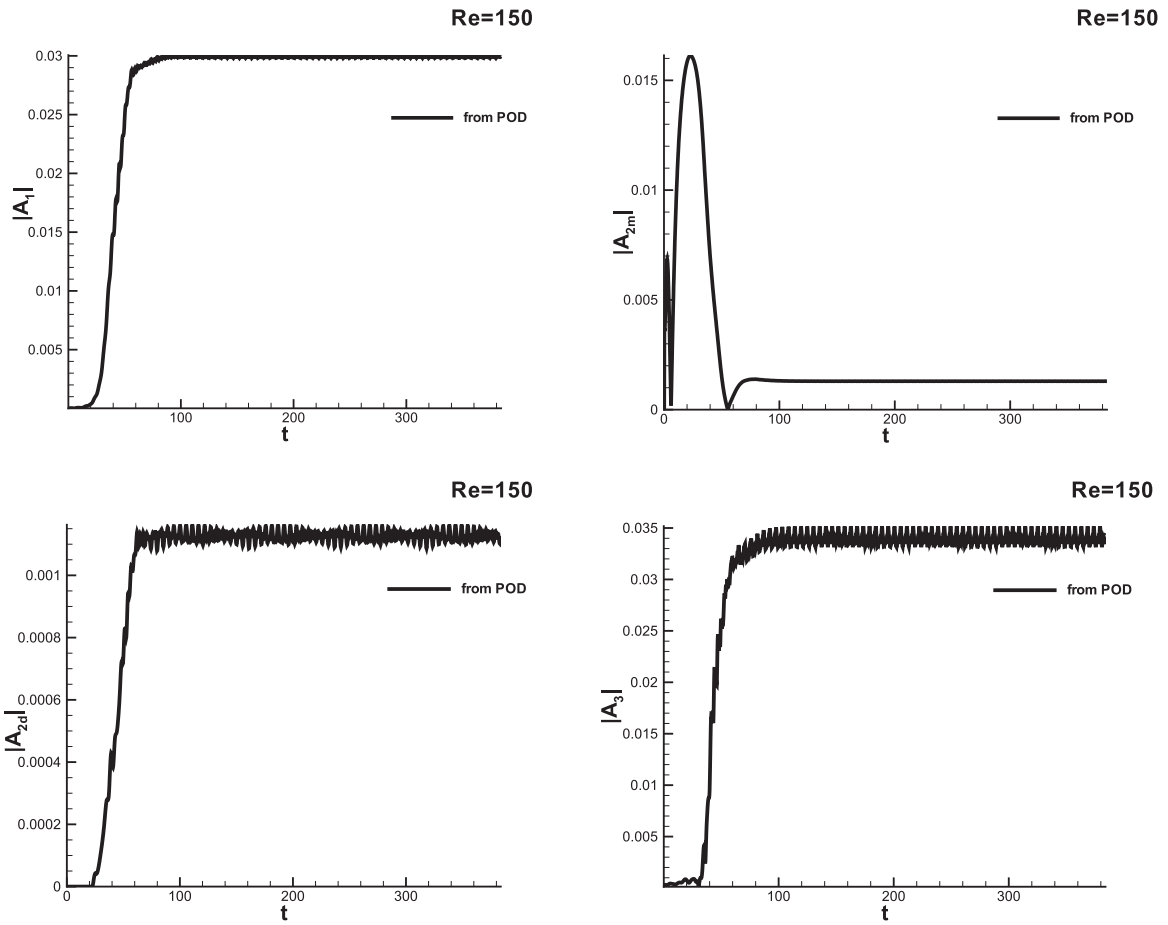

FIG. 12. Instability modes constructed for Re = 150 following the new representation of the T_1 mode.

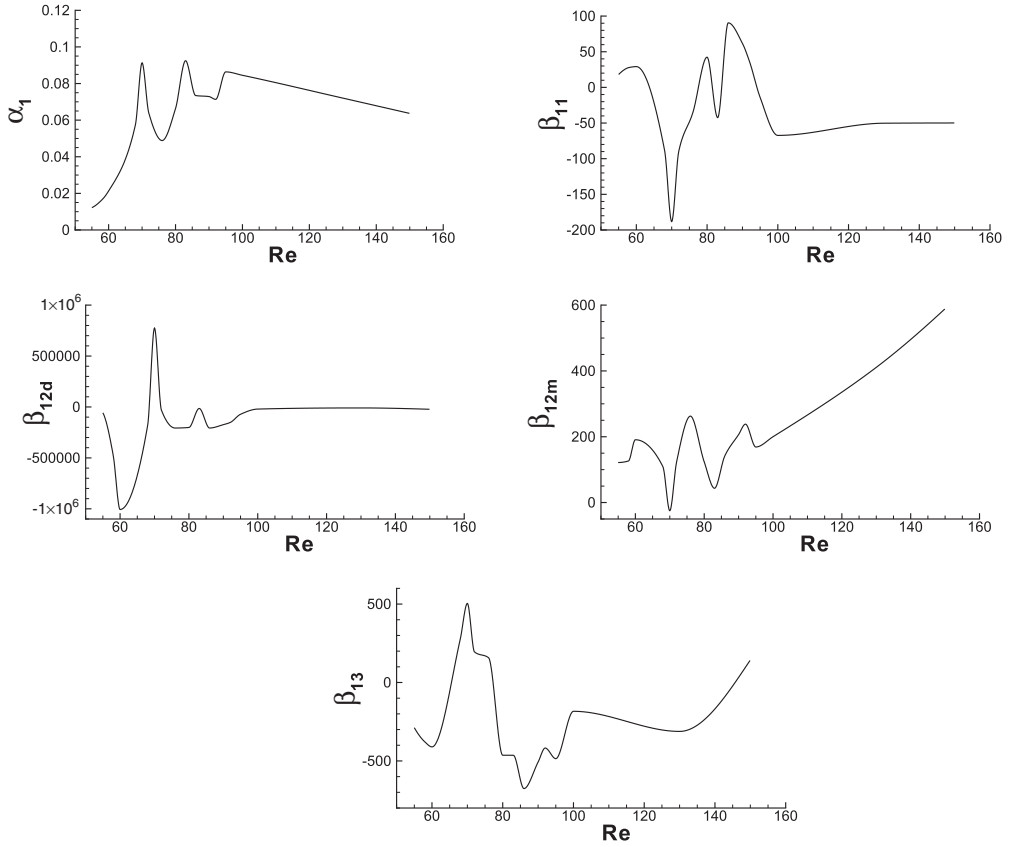

FIG. 13. Amplitude equation coefficients for A_1.

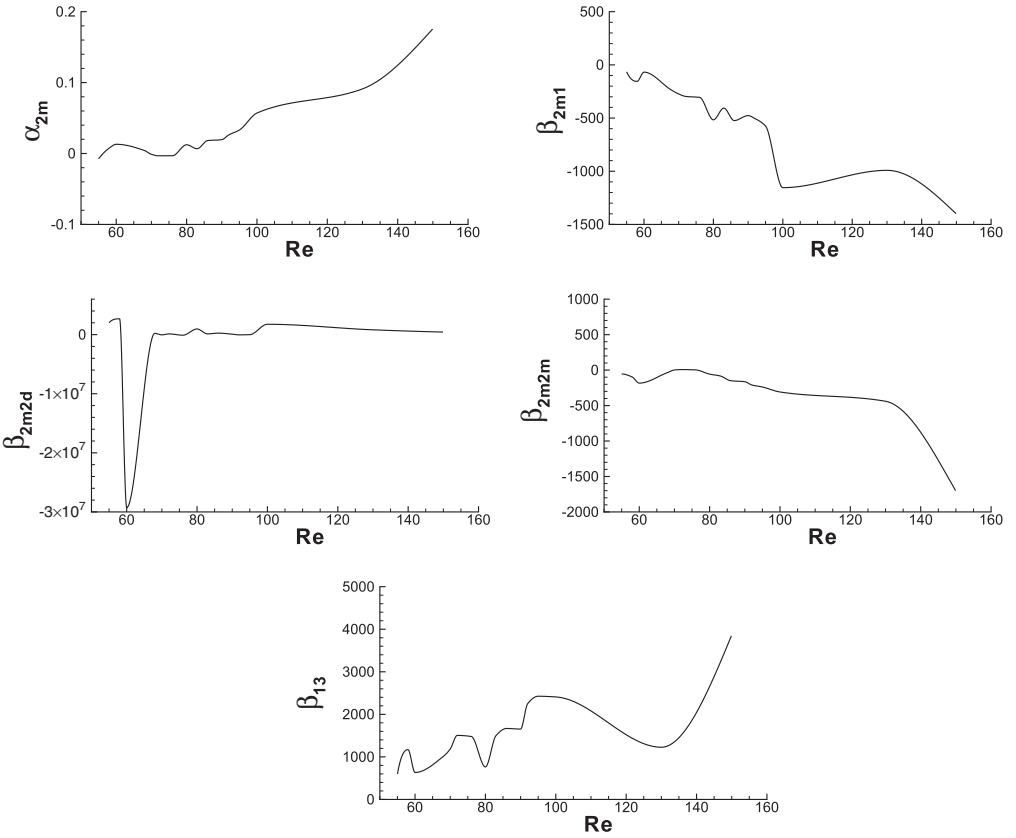

FIG. 14. Amplitude equation coefficients for A_{2m}.

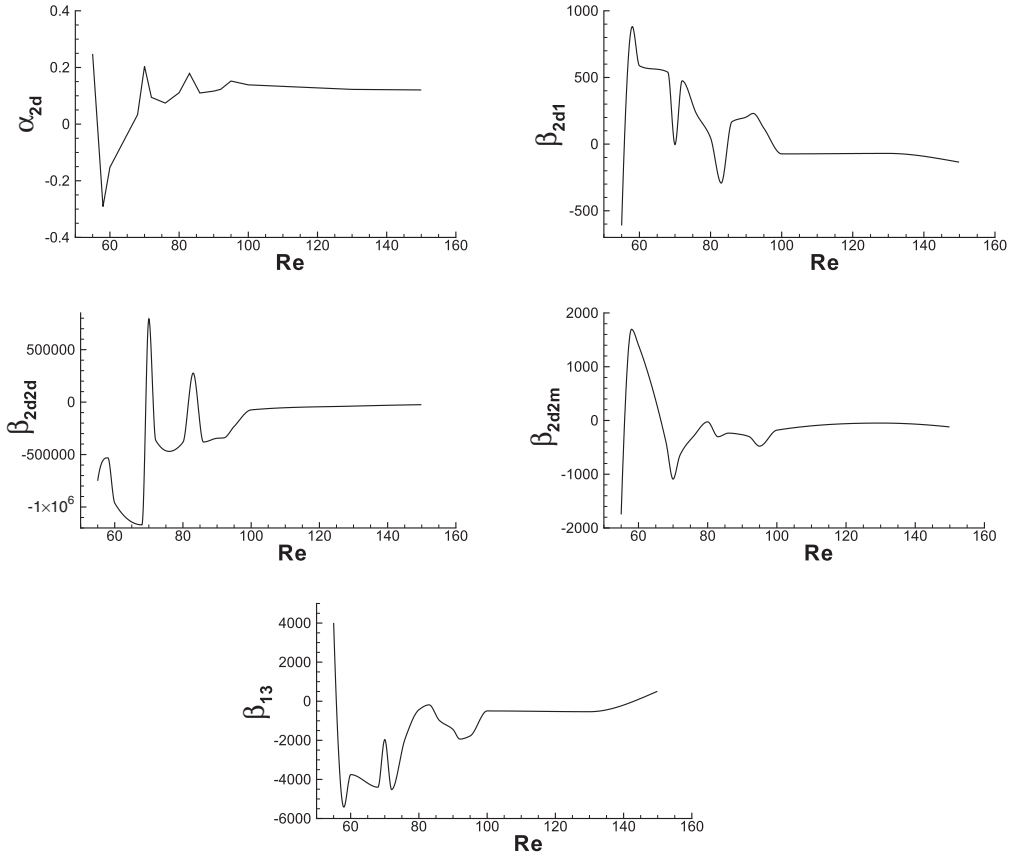

FIG. 15. Amplitude equation coefficients for A_{2d}.

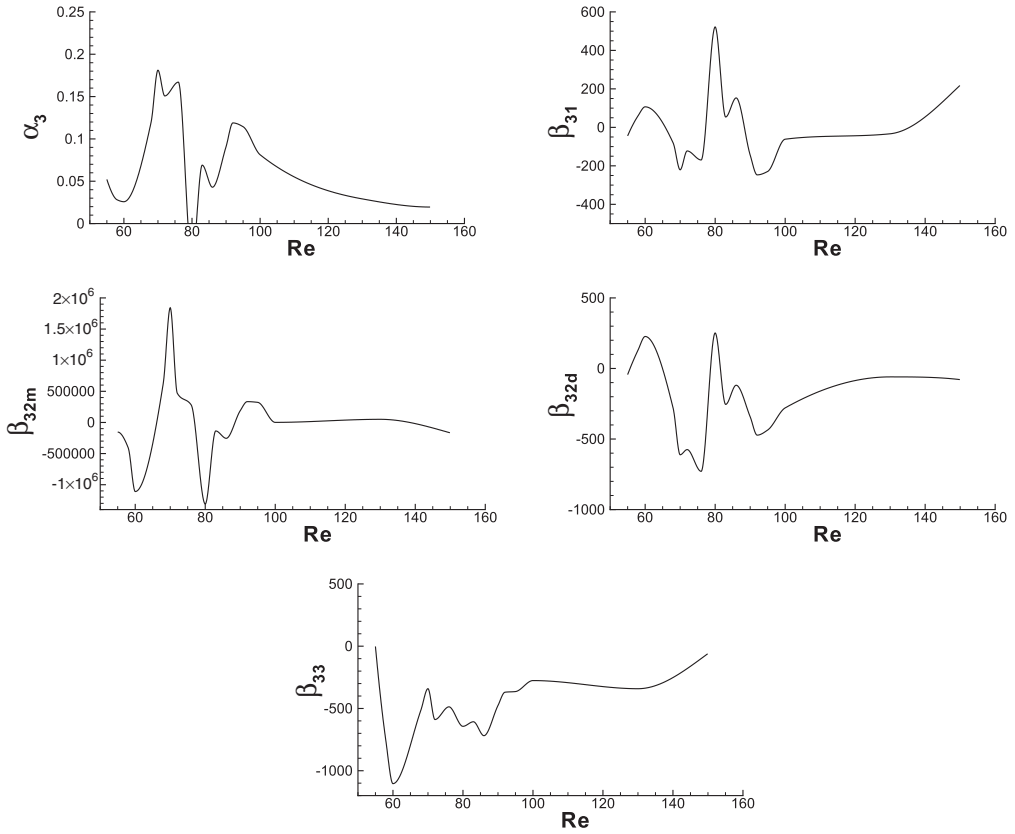

FIG. 16. Amplitude equation coefficients for A_3.

TABLE IV. Initial conditions for amplitude equations.

Re	$\lvert A_{10}\rvert$	$\lvert A_{2m0}\rvert$	$\lvert A_{2d0}\rvert$	$\lvert A_{30}\rvert$
100	8.1×10^{-5}	3.26×10^{-3}	8.0×10^{-7}	1.9×10^{-3}
130	3.46×10^{-5}	5.0×10^{-3}	1.69×10^{-6}	2.31×10^{-3}
150	2.5×10^{-5}	2.5×10^{-3}	2.1×10^{-6}	1.0×10^{-8}

For the case of Re = 150, T_{1r} is shown as a function of time in the middle frame of Fig. 11. A fast Fourier transform (FFT) of the rapidly varying component allows us to identify the dominant frequency (ω_d) of oscillation. Also, the amplitude envelope $T_{ra}(t)$ of the rapid variation of $T_{1r}(t)$ is found by first extracting the maxima and minima of every cycle and subsequently using a cubic Hermite interpolation to get the amplitude variation at intermediate time instants. Using the dominant frequency and the amplitude envelope information, the rapidly varying component is expressed as

$$T_{1r}(t) = T_{ra}(t)\cos(\omega_d t).$$

Using this representation, the instability mode $A_2(t)$ can now be defined as

$$A_2(t) = T_{1s}(t) + \frac{T_{ra}(t)}{2}\, e^{i\omega_d t}. \tag{28}$$

The phasor plot of $A_2(t)$ in the bottom frame of Fig. 11 shows the approach towards the limit cycle by the arrowhead starting from $\mathrm{Im}(A_2) = 0$. The thickness of the limit cycle is nonzero, but amplitude variation of $T_{ra}(t)$ is negligible. In formulating the SLE equations for this representation we split $A_2(t)$ into $A_{2m}(t)$, which accounts for the variation in mean and $A_{2d}(t)$ for the superimposed disturbance, as given by

$$A_{2m}(t) = T_{1s}(t), \tag{29a}$$

$$A_{2d}(t) = \frac{T_{ra}(t)}{2}\, e^{i\omega_d t}. \tag{29b}$$

The instability mode amplitude variations (A_1 to A_3) obtained using this approach are shown in Fig. 12 for Re = 150.

B. T_1-mode reconstruction

The new representation of the T_1 mode described above was implemented and used to reconstruct the SLE equations. The results given below are for Re = 100, while these are also available for Re = 130 and 150.

For the 3-mode $(A_1, A_{2m}, A_{2d}, A_3)$-SLE equations in the new formalism, the SLE equations have the following form for the amplitude:

$$\frac{d|A_1|}{dt} = \alpha_1|A_1| + \beta_{11}|A_1||A_1|^2 + \beta_{12m}|A_1||A_{2m}|^2 + \beta_{12d}|A_1||A_{2d}|^2 + \beta_{13}|A_1||A_3|^2, \tag{30}$$

$$\frac{d|A_{2m}|}{dt} = \alpha_{2m}|A_{2m}| + \beta_{2m1}|A_{2m}||A_1|^2 + \beta_{2m2m}|A_{2m}||A_{2m}|^2 + \beta_{2m2d}|A_{2m}||A_{2d}|^2 + \beta_{2m3}|A_{2m}||A_3|^2, \tag{31}$$

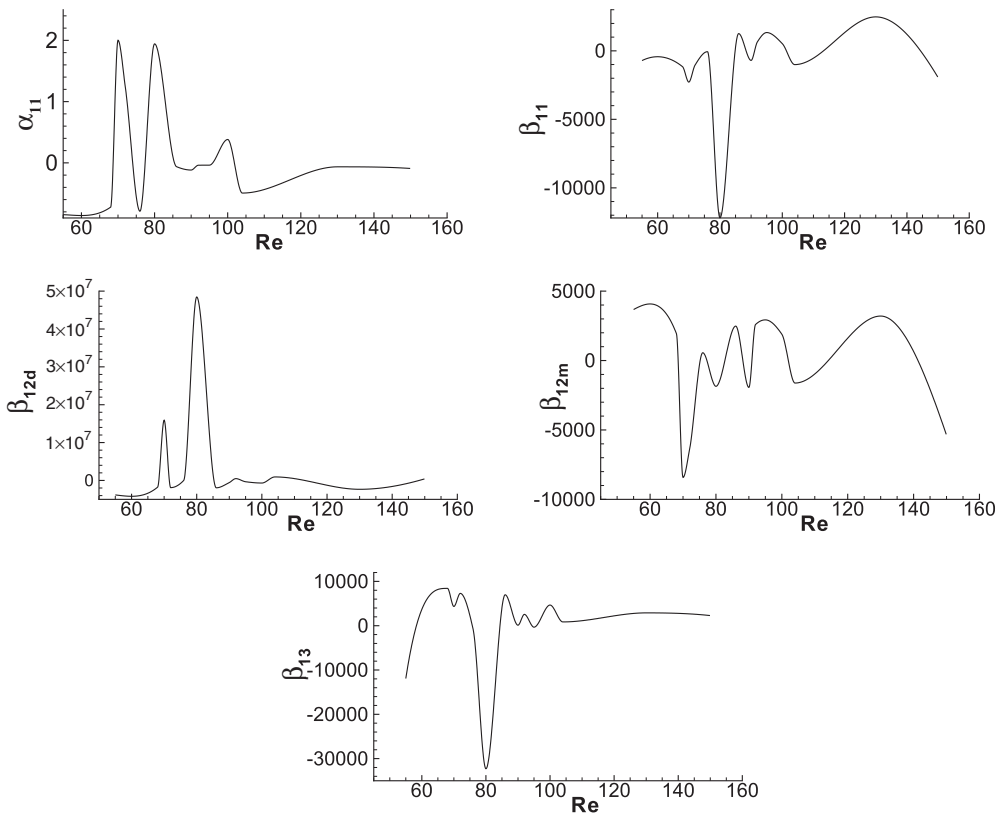

FIG. 17. Phase equation coefficients for θ_1.

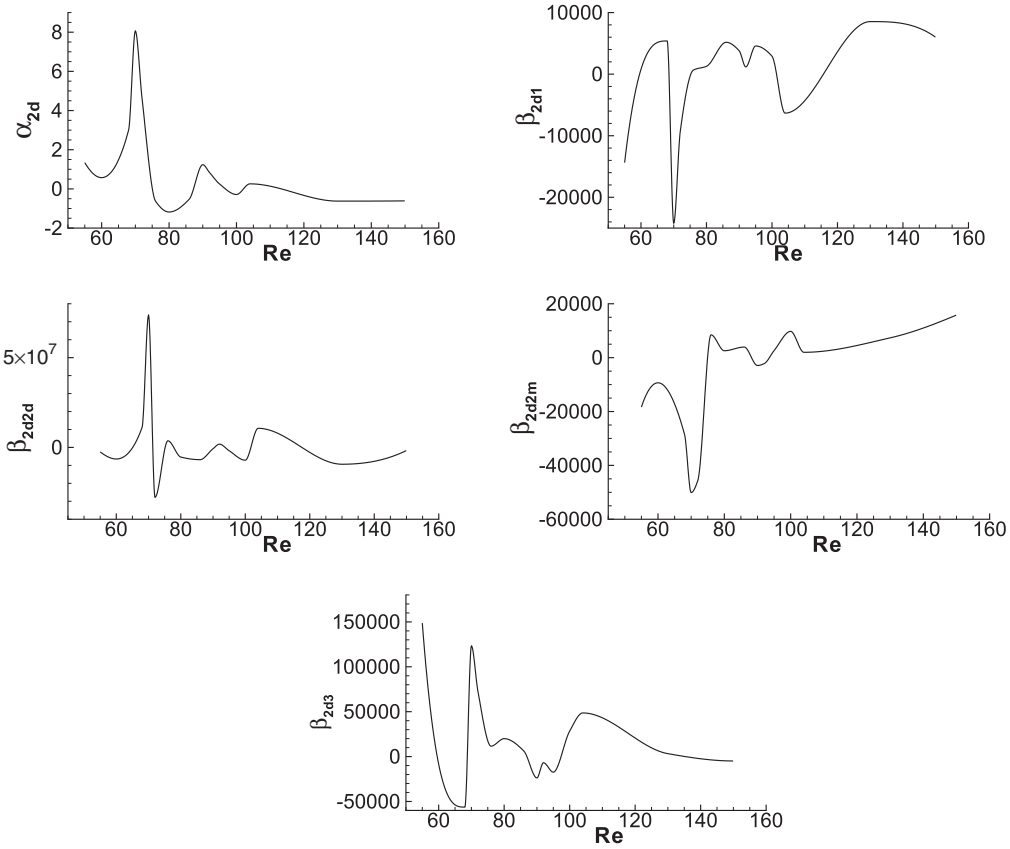

FIG. 18. Phase equation coefficients for θ_{2d}.

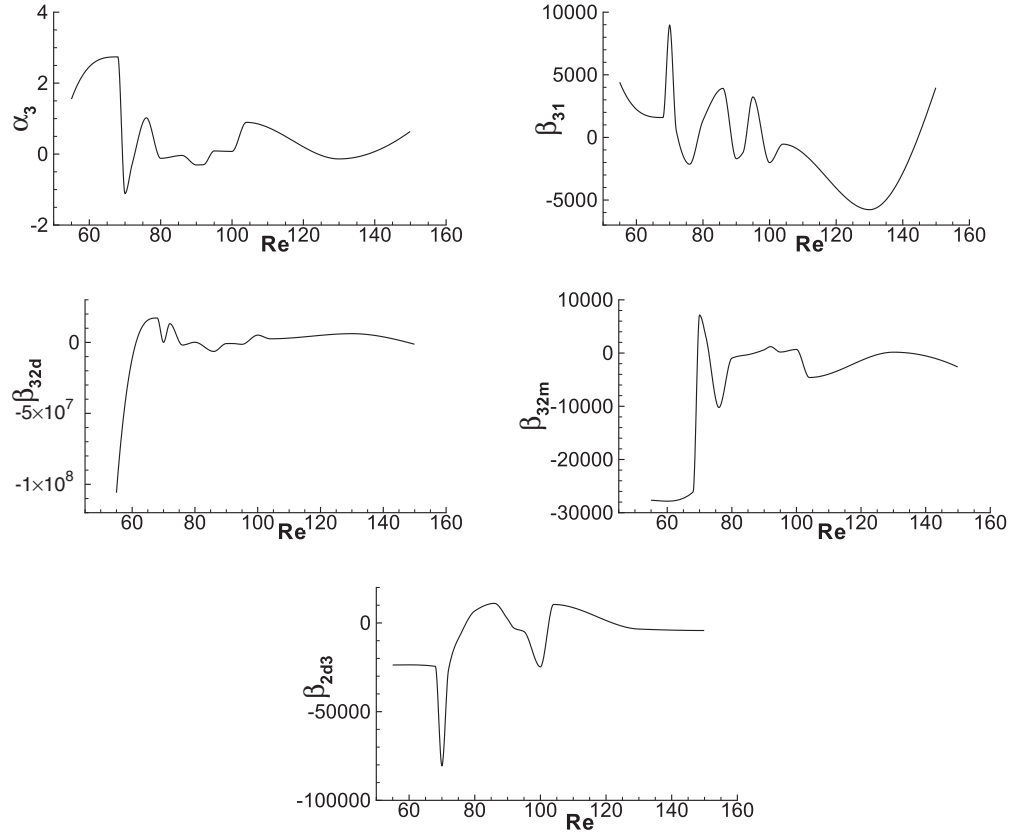

FIG. 19. Phase equation coefficients for θ_3.

$$\frac{d|A_{2d}|}{dt} = \alpha_{2d}|A_{2d}| + \beta_{2d1}|A_{2d}||A_1|^2 + \beta_{2d2m}|A_{2d}||A_{2m}|^2 + \beta_{2d2d}|A_{2d}||A_{2d}|^2 + \beta_{2d3}|A_{2d}||A_3|^2, \quad (32)$$

$$\frac{d|A_3|}{dt} = \alpha_3|A_3| + \beta_{31}|A_3||A_1|^2 + \beta_{32m}|A_3||A_{2m}|^2 + \beta_{32d}|A_3||A_{2d}|^2 + \beta_{33}|A_3||A_3|^2. \quad (33)$$

Note that the subscripts $2m$ and $2d$ relate to the interactions of the anomalous mode, as modeled here with other modes, including self-interaction. The coefficients of the amplitude equations obtained using the least squares approach for different Re′s are plotted in Figs. 13 to 16, with the coefficients identified.

The optimal initial conditions for the amplitudes are found through a time-integrated error analysis in the $(A_{10}, A_{2m0}, A_{2d0}, A_{30})$ hyperspace, similar to the approach stated above in Sec. VI, with the local minima in the $(A_{2m0}, A_{2d0}, A_{30})$ space found for different values of A_{10}, from which we determine the global minimum. The final global optimal initial conditions obtained by this process are given in Table IV.

The phase for 3-mode $(A_1, A_{2m}, A_{2d}, A_3)$-SLE equations are obtained from the solution of

$$\frac{d\theta_1}{dt} = \alpha_1 + \beta_{11}|A_1|^2 + \beta_{12m}|A_{2m}|^2 + \beta_{12d}|A_{2d}|^2 + \beta_{13}|A_3|^2, \quad (34)$$

TABLE V. Initial conditions for phase equations (in rad).

Re	θ_{10}	θ_{2m0}	θ_{2d0}	θ_{30}
100	− 9.409	0	− 9.685	12.410
130	1.257	0	8.45	0.944
150	1.606	0	11.210	− 6.147

$$\frac{d\theta_{2m}}{dt} = 0, \quad (35)$$

$$\frac{d\theta_{2d}}{dt} = \alpha_{2d} + \beta_{2d1}|A_1|^2 + \beta_{2d2m}|A_{2m}|^2 + \beta_{2d2d}|A_{2d}|^2 + \beta_{2d3}|A_3|^2, \quad (36)$$

$$\frac{d\theta_3}{dt} = \alpha_3 + \beta_{31}|A_1|^2 + \beta_{32m}|A_{2m}|^2 + \beta_{32d}|A_{2d}|^2 + \beta_{33}|A_3|^2. \quad (37)$$

The coefficients of the phase equations obtained using the same least squares approach as before are plotted in Figs. 17 to 19 for different Re′s.

As earlier, the initial conditions for phase are found graphically by averaging the difference in the reconstructed and the actual phase, with all phases initialized as zero. The optimal initial conditions thus obtained are given in Table V.

In Figs. 20 to 22, reconstructed amplitude and phase of instability modes are shown for Re = 100. In Fig. 20, one notices excellent match for the asymptotic values. A slight mismatch is noted during the transient phase, especially for A_{2m}. This is readily evident in Fig. 21, where the A_2 mode

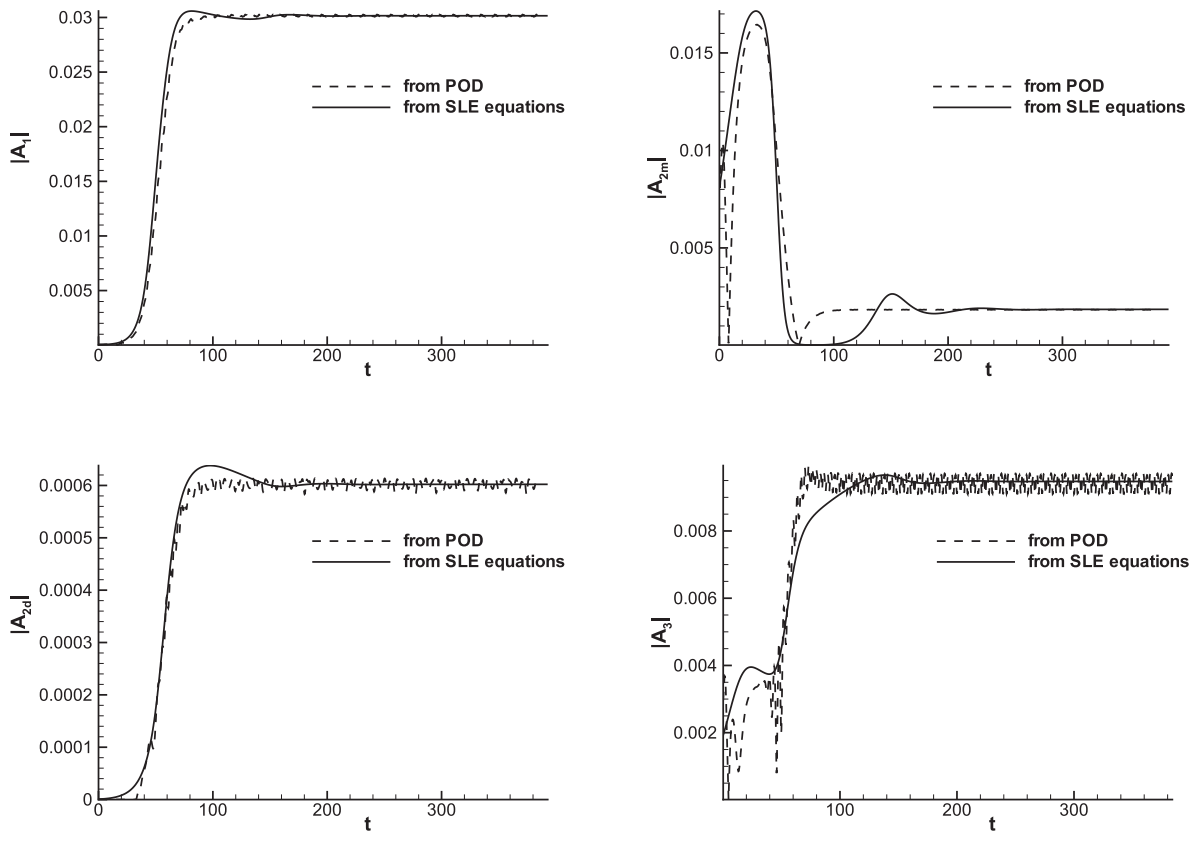

FIG. 20. Reconstructed instability mode amplitude variation with time for Re = 100.

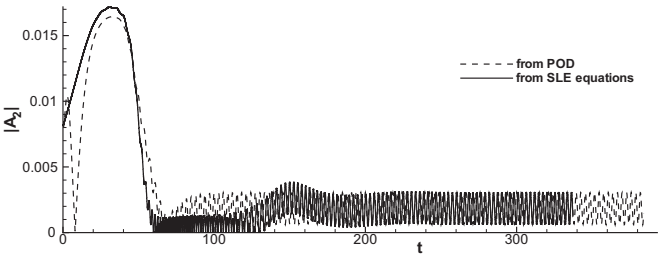

FIG. 21. Reconstructed A_2 mode amplitude variation with time for Re = 100.

is reconstructed following Eq. (28), which shows the match to be excellent beyond $t \approx 170$. The reconstructed phase in Fig. 22 for A_1, A_{2d}, and A_3 from SLE equations matches excellently with the data from POD performed with DNS data. In the following, we discuss cases for Re = 130 and Re = 150 without showing any figures for these cases.

For both the cases, instability modes' amplitude as obtained from the solution of SLE equation and that reconstructed from the POD data match even better with an increase in Reynolds number. One of the successes of the present effort is to reconstruct A_2, which belongs to T_1 modes. The phase matches rather well for all the Reynolds numbers. For Reynolds number equal to 150, the qualitative nature improved further, as compared to the case of Re = 130.

VIII. RECONSTRUCTION OF DISTURBANCE VORTICITY FROM THE SLE SOLUTIONS

Having obtained the amplitude and phase variation from the SLE equations, it is possible to get back the POD modes by tracing the steps required to construct SLE modes (from the POD modes) backward as given for R modes by

$$a_{2j-1}(t) = |A_j(t)| \cos\theta_j,$$
$$a_{2j}(t) = |A_j(t)| \sin\theta_j.$$

Care is needed to reconstruct the anomalous mode of the first kind (T_1) from the computed A_{2m}, A_{2d}, and θ_{2d}. We note that in computing the modulus of the slowly varying component (T_{1s}) mode, we lose the information of its sign. Therefore, in reconstructing the T_1 mode from $|A_{2m}|$, this information on sign is provided explicitly by comparing with the original T_1 mode in POD representation.

For the T_1 mode,

$$a_{2j-1}(t) = A_{jm}(t) + 2|A_{jd}(t)| \cos\theta_{jd}.$$

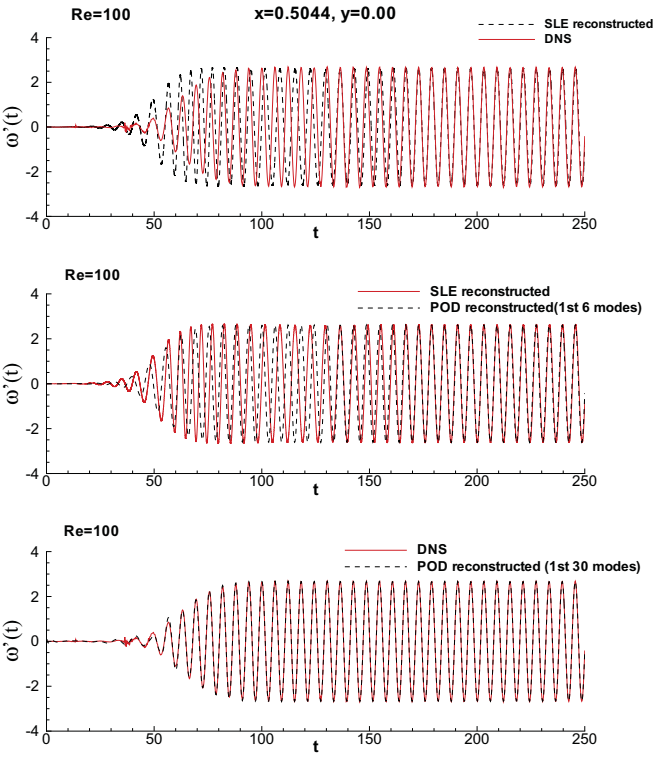

FIG. 23. (Color online) Disturbance vorticity obtained from DNS reconstructed using the results from the SLE equations for Re = 100 at (0.5044, 0.0).

Subsequently, these POD modes can be utilized to reconstruct the disturbance vorticity at any point in the flow field. The reconstructed disturbance vorticity at two points, one along the centerline of the wake (0.5044, 0) and another at 45° with respect to the centerline at (1.016, 1.016), are presented in Figs. 23 and 24.

In Fig. 23, the reconstructed disturbance vorticity data from the solution of SLE equations for the 3-mode case is shown for Re = 100 at a point in the near wake ($x = 0.5044$, $y = 0.0$). The figure shows comparison between DNS data with this 3-mode SLE reconstruction. It is very apparent that for $t \geqslant 90$ the match between the two is almost perfect. The match appears natural except for the choice of initial condition, which can cause a mismatch. Higher than 3-mode SLE equation reconstruction would be tedious to track the optimal initial conditions. Even for the 3-mode model developed here, an optimal search required locating the global minimum in a

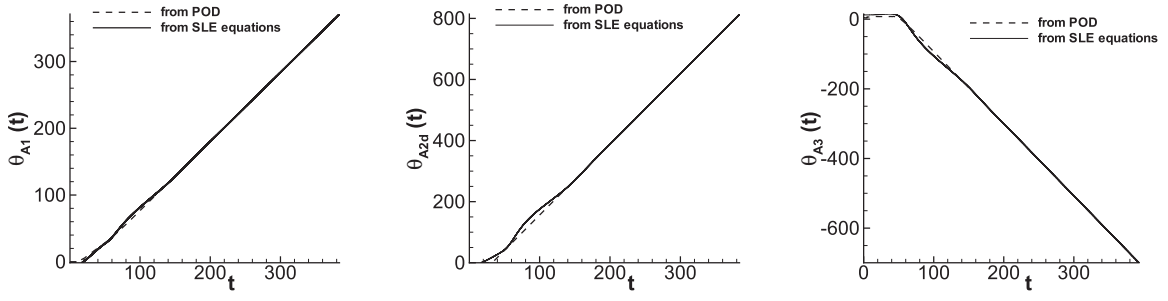

FIG. 22. Reconstructed phase variation with time of the instability modes for Re = 100.

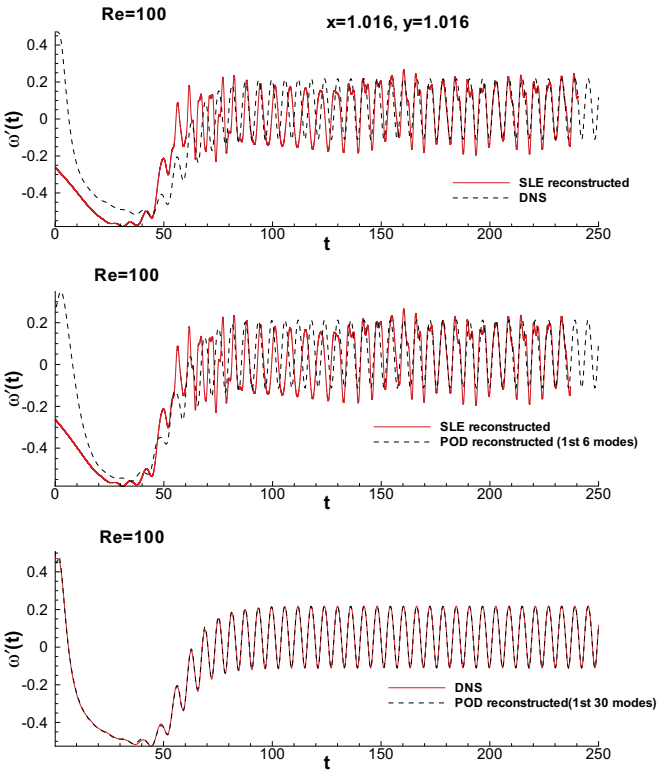

FIG. 24. (Color online) Disturbance vorticity obtained from DNS reconstructed using the results from the SLE equations for Re = 100 at (1.016, 1.016).

four-dimensional space. This problem will be present for higher than 3-mode SLE models; however, it is eminently solvable.

While the match between ROM based on SLE equations and DNS data show remarkable accuracy in Fig. 23, the same is investigated for another point which is located in the near wake, but is off-center. This comparison is shown in Fig. 24 using the same 3-mode SLE reconstruction strategy. It is readily evident that the 3-mode ROM matches with DNS data very well asymptotically, as shown in these figures. From the eigenfunctions shown in Fig. 2, one notices that the modal contributions on off-center points are asymmetric with respect to the centerline. This will lead to higher mismatch with the POD data, due to higher sensitivity of phase match from the solution of Eqs. (34) to (37) for any off-center point.

IX. SUMMARY AND CONCLUSION

In the present research, the following have been achieved.

(1) POD modal decomposition and projecting these onto instability modes have been performed for flow past a circular cylinder at multiple supercritical Reynolds numbers, with results shown in Figs. 1, 2, and 4–7. While enstrophy-based POD analysis has been shown earlier for vortex-dominated flows in [1,11], and here the generality of this approach needs to be established for other flows. Some preliminary results for flow past a flat plate undergoing transition to turbulence has been reported in [12].

(2) Modeling cylinder wake by the SL and SLE equations is an important exercise. The superiority of the SLE equation over the SL equation has been already noted in [1]. However, finding the coefficients of the SLE equation is not a straightforward proposition. In the present work the deterministic route [1] has been replaced by a least squares approach for the generality it affords. The success of reconstructing the disturbance vorticity by the present approach is a proof of robustness of the proposed ROM.

(3) Another important aspect of ROM is the choice of initial condition for the developed SLE equations, as these equations are stiff ordinary differential equations. The sensitivity of a stiff differential equation on initial conditions has been explored here rationally and the choice of initial condition is explained with the help of Figs. 8 and 9.

(4) An accurate representation of enstrophy-based POD of flows also reveals the presence of modes which occur in isolation [1,11] and is shown here also. The traditional approach of treating instability modes by SL or SLE equations does not work directly due to the isolated nature of the corresponding POD modes with higher frequencies. Quantifying the effects of this via the time-averaged Navier-Stokes equation fails to capture these high frequency variations. Here this aspect has been captured using DNS data in modeling this anomalous mode of first kind (T_1 mode) by a multi-time-scale approach with results shown in Figs. 11 and 12. This exercise reveals the actual physics of instability for flow past a cylinder.

(5) Reconstructed 3-mode ROM solutions (shown in Figs. 20–22) and disturbance vorticity from DNS (in Figs. 23 and 24) match globally in the flow field. Thus, we have successfully converted the problem of solving the Navier-Stokes equation into solving three complex ordinary differential equations. This will lead to very accurate solutions at supercritical Reynolds number flows by investigating a few minutes, instead of hundreds of CPU hours of larger clusters using high performance computing. Once achieved, this will be a path-breaking achievement in ROM of bluff body flows.

(6) The present exercise highlights the physical role played by the anomalous modes for this flow, by relating POD and instability modes. Apart from explaining the role of this anomalous mode (T_1 mode) in taking the dynamical system to a new equilibrium state characterized by vortex shedding, the presented ROM will help control such flows by suppressing vortex shedding [18], an exercise useful for both scientific and technological reasons.

[1] T. K. Sengupta, N. Singh, and V. K. Suman, J. Fluid Mech. **656**, 82 (2010).

[2] G. K. Batchelor, *Introduction to Fluid Mechanics* (Cambridge University Press, Cambridge, UK, 1988).

[3] L. D. Landau and E. M. Lifschitz, *Fluid Mechanics* (Pergamon Press, New York, 1959), Vol. 6.

[4] F. Homann, Forsch. Ingenieurwes. **7**, 1 (1936).

[5] H. Schlichting, *Boundary Layer Theory* (McGraw Hill, New York, 1987).
[6] M. Provansal, C. Mathis, and L. Boyer, J. Fluid Mech. **182**, 1 (1987).
[7] K. R. Sreenivasan, P. J. Strykowski, and D. J. Olinger, in *Forum on Unsteady Flow Separation*, edited by K. N. Ghia (ASME, New York, 1987), pp. 1–13.
[8] C. H. K. Williamson, J. Fluid Mech. **206**, 579 (1989).
[9] E. Akervik, L. Brandt, D. S. Henningson, J. Hoepffer, O. Marxen, and P. Schlatter, Phys. Fluids **18**, 068102 (2006).
[10] T. K. Sengupta and R. Sengupta, Comput. Mech. **14**, 298 (1994).
[11] T. K. Sengupta, N. Singh, and V. V. S. N. Vijay, Comput. Fluids **40**, 221 (2011).
[12] T. K. Sengupta, S. Bhaumik, and Y. G. Bhumkar, *6th AIAA Theoretical Fluid Mechanics Conference, Honululu, Hawaii, USA, 27–30 June* (2011).
[13] C. Rowley, I. Mezić, S. Bagheri, P. Schlatter, and D. S. Henningson, J. Fluid Mech. **641**, 1 (2009).
[14] P. J. Schmid, J. Fluid Mech. **656**, 5 (2010).
[15] M. S. Hemati, M. O. Williams, and C. W. Rowley, Phys. Fluids **26**, 111701 (2014).
[16] J. H. Tu, C. W. Rowley, D. M. Luchtenburg, S. L. Brunton, and J. N. Kutz, J. Comput. Dyn. **1**, 391 (2014).
[17] K. K. Chen, J. H. Tu, and C. Rowley, J. Nonlinear Sci. **22**, 887 (2012).
[18] A. Dipankar, T. K. Sengupta, and S. B. Talla, J. Fluid Mech. **573**, 171 (2007).
[19] B. R. Noack, K. Afanasiev, M. Morzynski, G. Tadmor, and F. Thiele, J. Fluid Mech. **497**, 335 (2003).
[20] D. D. Kosambi, J. Indian Math. Soc. **7**, 76 (1943).
[21] K. Karhunen, Ann. Acad. Sci. Fenn. Ser. A1, Math. Phys. **34**, 1 (1946).
[22] M. Loéve, C. R. Acad. Sci. Paris **220** (1962).
[23] K. Pearson, Philos. Mag. **2**, 559 (1901).
[24] P. Holmes, J. L. Lumley, and G. Berkooz, *Turbulence, Coherent Structures, Dynamical Systems and Symmetry* (Cambridge University Press, Cambridge, UK, 1996).
[25] L. Sirovich, Q. Appl. Math. **45**, 561 (1987).
[26] X. Ma. and G. E. Karniadakis, J. Fluid Mech. **458**, 181 (2002).
[27] A. E. Deane, I. G. Kevredekis, G. E. Karniadakis, and S. A. Orszag, Phys. Fluids A **3**, 2337 (2002).
[28] D. Rempfer and H. Fasel, J. Fluid Mech. **260**, 351 (1994).
[29] P. G. Drazin and W. H. Reid, *Hydrodynamic Instabilities* (Cambridge University Press, Cambridge, UK, 1981).
[30] L. D. Landau, C. R. Acad. Sci. URSS **44**, 311 (1944).
[31] J. T. Stuart, J. Fluid Mech. **9**, 353 (1960).
[32] T. K. Sengupta, *Instabilities of Flows and Transition to Turbulence* (CRC Press, Boca Raton, FL, 2012).
[33] T. K. Sengupta, *High Accuracy Computing Methods: Fluid Flows and Wave Phenomena* (Cambridge University Press, Cambridge, UK, 2013).
[34] T. K. Sengupta, M. K. Rajpoot, and Y. Bhumkar, Comput. Fluids **47**, 144 (2011).
[35] H. A. Van der Vorst, SIAM J. Sci. Stat. Comput. **12**, 631 (1992).
[36] T. K. Sengupta, H. Singh, and S. Bhaumik, Comput. Fluids **88**, 440 (2013).
[37] T. K. Sengupta, S. Dey, and S. Sarkar, J. Fluid Mech. **493**, 227 (2003).
[38] T. K. Sengupta and S. De, Comput. Struct. **82**, 2963 (2004).
[39] M. Morzynski, K. Afanasiev, and F. Thiele, Comput. Meth. Appl. Mech. Eng. **169**, 161 (1999).
[40] S. G. Siegel, J. Seidel, C. Fagley, D. M. Luchtenberg, K. Cohen, and T. McLaughlin, J. Fluid Mech. **610**, 1 (2008).
[41] B. R. Noack, M. Schlegel, M. Morzynski, and G. Tadmor, Int. J. Numer. Meth. Fluids **63**, 231 (2010).
[42] B. R. Noack and R. Niven, Comput. Math. Appl. **65**, 1558 (2013).
[43] P. J. Strykowski, Ph.D. dissertation, Yale University, New Haven, CT, 1986.
[44] P. J. Strykowski and K. R. Sreenivasan, J. Fluid Mech. **218**, 74 (1990).
[45] W. Eckhaus, *Studies in Nonlinear Stability Theory* (Springer Verlag, Berlin, 1965).
[46] S. Bhaumik, S. Sengupta, and A. Sengupta, Comput. Fluids **81**, 110 (2013).